https://dx.doi.org/10.1016/j.jcsr.2021.107061

Material properties and residual stresses of high strength steel hexagonal hollow sections

Jun-zhi Liu[1]; Han Fang[2]; Shuxian Chen[1]; Tak-Ming Chan[1, *]

1 Department of Civil and Environmental Engineering, The Hong Kong Polytechnic University, Hong Kong, China
2 School of Civil, Environmental and Mining Engineering, The University of Adelaide, South Australia 5005, Australia
* Corresponding author: tak-ming.chan@polyu.edu.hk

Abstract

This paper presents an experimental investigation on the material properties variation and residual stress distribution within the high strength steel (HSS) hexagonal hollow sections. Three different fabrication routes encompassing welding or combinations of welding and press-braking were used for fabricating the HSS hexagonal sections. HSS plates of grade Q690 with two thicknesses of 6 mm and 10 mm were employed. A total of 76 tensile coupons extracted from the parent plates and the hexagonal hollow sections with different fabrication routes were tested to obtain the static material properties of the parent steel plates and the material properties variation for the hexagonal hollow sections. A new material model describing the material properties for the flat portion was proposed while the existing material model for cold-formed steel was modified for the materials at the press-braked corners. In addition, residual stresses measurements for five HSS hexagonal sections with different fabrication routes and varying section slenderness were subsequently performed. Sectioning method was adopted in this study with 74 strips extracted and more than 898 strain readings obtained. Results of the residual stress distributions and the magnitudes are presented and discussed. Based on the measurement results, predictive models for residual stresses were developed and can be applied to estimate residual stresses for predicting the structural behaviour of the HSS hexagonal hollow sections.

Keywords: High strength steel; hexagonal sections; fabrication routes; Material properties; Residual stresses.

1. Introduction

High strength steel (HSS) (nominal yield strength $f_y \geqslant$ 460 MPa) tubular structures have been increasingly utilized in civil and structural applications due to their high strength-to-weight ratios [1], good buckling resistance [2], aesthetic appearance and ease of transportation and erection [3]. To employ these HSS structures to form civil infrastructures, the characteristics of material properties and residual stresses of HSS structures as well as understanding of the structural performance under various loading conditions are required. Existing research on the residual stresses for HSS is relatively limited in comparison with mild steel [6]. Moreover, the research performed for HSS hexagonal and octagonal hollow sections is limited. Owing to the higher buckling resistance of hexagonal and octagonal section structures which also allow for easier connection construction with incoming members, the application of these structures in buildings and infrastructures has gained increasing popularity [8, 22]. However, the research regarding the HSS hexagonal sections is fairly scarce. To generate accurate design and analysis of the structures, the material properties and residual stresses for the HSS hexagonal hollow section structures need to be investigated.

Existing experimental and numerical investigations regarding hexagonal hollow sections made from conventional steel plates were reported in [9-13]. In the study of Aoki et al. [9], the hexagonal hollow sections specimens were fabricated by welding six steel plates, as depicted in Fig. 1(a). The HSS hexagonal hollow sections can also be fabricated using two half cold-formed sections with each featured two bent-corners and the welding is operated at the corner, see figure Fig. 1(b). A different fabrication route involving cold-forming processes was used by Mitiga et al. [10] and Evirgen et al. [11]. The specimens in these studies [10-11] were produced using two cold-formed half-sections which were subsequently welded to form the hexagonal hollow sections. Each half-section has three bent-corners and the welding seams locate on the flat portion, as shown in Fig 1(c). These different fabrication routes can induce heterogeneity of material, residual stresses and geometrical imperfections, all of which would influence the behaviour of the structures [14-17]. The welding fabrication process induces residual stresses due to strain misfit when welding material solidifies [18]. Besides, the heat-affected zone (HAZ) generated from the induced heat input of welding would adversely influence the structural behaviour since the material inside HAZ would be significantly altered [24, 25], causing premature yielding and stiffness loss to the HSS tubular members, invariably leading to great level of deterioration of loading bearing capabilities. Cold-forming process including the cold-rolling and press-braking essentially resulted in altered material properties at the cold-formed regions due to the excessive strain-hardening at cold-formed regions with significant plastic deformation [19-23]. However, no investigations have been conducted on the material properties and residual stresses of the HSS hexagonal hollow sections fabricated with welding and cold-forming processes.

In order to have comprehensive understanding of the material properties and residual stresses of HSS hexagonal hollow sections, the structures with different fabrication routes need to be considered. In this study, the material properties of the HSS hexagonal hollow section manufacturing from three different fabrication routes were investigated. HSS hexagonal hollow sections with a range of plate width-to-thickness ratios were fabricated. Tensile coupon tests on specimens extracted from the parent HSS plates and at different locations across the HSS hexagonal hollow sections were performed. Based on the results, the influence of fabrication processes on the variation of mechanical properties is discussed. Stress-strain models, which can accurately capture the material behaviour for the stress-strain curves both featured with yield plateau and relatively rounded responses, were developed. In addition, the distribution of the residual stresses in HSS hexagonal hollow sections formed using different fabrication routes were also measured and compared. The effect of fabrication routes on the distribution pattern is discussed. Predictive models for residual stress distribution are also provided based on the measured results.

2. HSS Hexagonal hollow section specimens

HSS hexagonal hollow sections, for the current study were fabricated using Q690 steel plates with two nominal thicknesses of 6 mm and 10 mm, as shown in Fig. 2. The initial Q indicates the nominal yield strength in accordance with Chinese code terminology and it was delivered in Quenched and Tempered (QT) condition. The chemical composition of the HSS plates are shown in Table 1, and the comparisons with EN 10025-6 [118] illustrate that HSS plates are qualified. To allow for direct comparison, the Q690 steel plates were manufactured from the same batch with same furnace number and chemical composition, as shown in Table 1 with carbon equivalent value (CEV) indicating the weldability of steel as high carbon equivalent value (>0.43) generally indicates poor weldability [39]. The sections of W-145 × 6, CF1-145 × 6, CF2-145 × 6, CF2-200 × 6 and CF2-145 × 10 sections encompassing three fabrication routes were employed to examine the material properties variation within the cross section. The detailed geometries of the examined specimens are tabulated in Table 2 with plate width to thickness ratio (b/t) ranging between 12.6 and 30.3. The HSS hexagonal sections are labelled as "Fabrication route, nominal width (B) and thickness", in which "W" refers to the first series with six plates welded together [Fig. 1(a)], "CF-1" refers to the two cold-formed sections with each half with two bent-corners [Fig. 1(b)] and "CF-2" indicates the two cold-formed parts which are welded together with each half featuring three bent-corners [Fig. 1(c)].

For the W-series specimens, the six HSS plates were welded together using gas metal arc welding (GMAW) after filling the ceramic backing at corner. The gas metal arc welding process (GMAW) is one of the commonly used processes in bridge construction because of its productivity and high deposition rates [40]. Full penetration weld was used with 1.2 mm electrode of ER110S-G category (f_y = 860 MPa, f_u = 920 MPa) in accordance with the specification AWS A5.28/5.28 M [38], and the chemical composition of the electrode is given in Table 3. The shielding gas was mainly composed of 80% Argon (Ar) with remaining volume filled with 20% carbon dioxide (CO_2) of 10 MPa filling pressure. The voltage, current and the welding speed were carefully controlled and recorded to determine the line heat input energy, which can be derived based on Eq. (1). Line heat input energy is an important controlling parameter which can influence the mechanical properties of the heat affected zone (HAZ) of a welded section [116, 117]. It is defined as the per unit length heat input generated during the welding process.

$$Q = \frac{k \times U \times I \times 60}{v \times 1000} \qquad (1)$$

where k is the thermal efficiency taken as 0.8 for GMAW [23, 28] U is the welding voltage in volt (V), I is the welding current in ampere (A), and v is the welding speed in millimeter per minute (mm/min). The current was varied between 120 A and 130 A while the voltage is between 19 V and 21 V with welding speed taking as average of the recording time as 120 mm/min, whereby linear heat input of between 0.91 kJ/mm and 1.09 kJ/mm can be obtained.

While fabricating the specimens for the CF-1 and CF-2 series, steel plates were longitudinally folded at the room temperature through press-braking, as shown in Fig. 3. To avoid the cracks along the bending area, the inner radius of the corner to thickness ratio should be designed in accordance with the specifications. The inner radius of the corner to thickness applied for the investigated specimen in this paper is 3. It should be noted that the inner bending corner radius to thickness ratio remarkably indicates the level of plastic deformation and the susceptibility to brittleness due to press-braking. The manufacturing requirements for outer corner radius to thickness ratio is regulated among countries and regions. EN 10219-2 [105], ASTM/A1085 [107], GB/T 6728 [108] AS/NZS 1163 [109], JIS G 3128 [111]and ISO 14346 [115] generally specify comparable requirements on outer corner radius to thickness ratio varied between 1.6 t and 3.5 t with minimum ratio equal to 1.6 t regulated in ASTM/A1085. The provision of JIS G 3101 [110] specifies the strictest limit value of 3.0 t. Aside from the lower bound specified in provisions, specification of ASTM A500 [106], JIS G3466 [112] and CSA G40.20-13 [113] stipulate the maximum value of corner to thickness ratio only to allow for large usable flat portion for the ease of construction. Since the process of press-braking is directly associated with the inner ratio of the corner radius to thickness ratio, the specified value of outer corner to thickness ratio is transformed to inner corner corner to thickness ratio as shown in Table 4.

3. Non-destructive inspection

The HSS plate is characterized with brittle nature since the ductility decreases with increasing material strength [4]. Wang et al. [26] observed that the crack can appear when the inner radius to thickness ratio is lower than 2.5, increasing the susceptibility to brittleness due to press-braking. Thus, the crack near the cold-bending areas and the HAZ induced crack in weldment particular in the vicinity of corner welding are examined using non-destructive methods.

3.1 Radiographic evaluation of GMAW by X-ray

Radiographic testing (RT) is commonly used as an industrial non-destructive testing method to ensure the quality of the structural element. Conventional RT utilizes chemical-based photographic film for recording the defects in the structures. The latent image is converted into a visible image through the chemical processing in dark room, which is formed in the emulsion layer of the film as per ASTM E94 00 [29]. Industrial X-ray source offers higher exposure rates and reduced exposure time in comparison with gamma source, as seen in Fig. 4. The evaluation of the welded areas in the structural components is essential [30] as per part of quality control requirements of the codes and standards GB 50205 [31]. Therefore, the X-ray inspection was performed in accordance with GB/T 3323.1 [32] and ISO 17636-1 [33]. The results are assessed in line with the specification codified in GB 50661 [34]. Sensitivity requirements specified in Article 2 of ASME Sec V are complied with and the radiographs have been evaluated as per ASTM E 2002 [35]. From the evaluation, no crack, porosity, undercut and slag inclusion etc. were observed from the welding in the specimens, as represented in Fig. 5.

3.2 Magnetic particle inspection method for surface crack detection

Concerning the possibility of the appeared crack in the vicinity of corner regions formed by press-braking, magnetic particle inspection method was also employed to inspect the existence of the crack. An AC electromagnetic yoke was utilized to generate AC magnetic field for the detection of surface indications during magnetic particle testing similar to the investigation performed by Goebbels [36] A bright white, opaque non-destructive testing (NDT) contrast paint, which provides a high contrast background to improve detection and sensitivity during visible magnetic particle inspections, was utilized and sprayed evenly without flaking. Hence, the indications appear clearly against the opaque white background after the application of coloured magnetic particle [37]. The result of the surface detection can be seen in Fig. 6 where no cracks were observed near the press-braked corner.

4. Material properties investigation

4.1 Tensile coupon tests

In order to investigate the variation of the material properties and the material heterogeneity induced by different fabrication processes, the longitudinal tensile coupons taken from the flat and corner portions of the HSS hexagonal hollow sections, were prepared for the investigation. Six flat coupons were taken from each batch of the steel plate in the longitudinal and transverse directions, as shown in Fig. 7. Steel plates with nominal yield strength of 690 MPa and thicknesses of 6 mm and 10 mm were employed in this study for fabricating the HSS hexagonal hollow sections using the three fabrication routes and categorised as W-series, CF1-series and CF-2 series, as described in section 2. A total of 76 tensile coupon tests were conducted whereas 6 flat coupons were machined from the parent plates with three for each plate thickness. 41 flat coupons were extracted from flat portions of the HSS hexagonal hollow sections while 19 corner coupons were extracted from the corner regions of the HSS hexagonal sections. For the four HSS hexagonal hollow sections, 4 coupons containing the weldment are also milled to investigate the effect the welding and HAZ effect.

4.1.1 Flat coupon tests

The flat coupons from the HSS hexagonal sections were extracted from the centre of the flat portion of the specimens. All the coupon tests were conducted in accordance with the international code EN ISO 6892-1: 2019 [38] using an in-house electromechanical high force universal testing system of Instron 5982 testing machine with a capacity of 100 kN, as shown in Fig. 8. The dimensions of the flat coupons conformed to the EN 6892-1: 2019 [38], and with 13 mm and 8 mm width along the gauge length respectively for 6 mm and 10 mm thick specimens. According to EN ISO 6892-1:2019 [38], the proportional elongation at fracture (ε_f) is based on an original gauge length of $5.65\sqrt{A}$, where A is cross sectional area along the parallel original gauge length of the coupon. For each coupon, the original gauge length was marked by fine lines before testing.

The test arrangement of the flat tensile coupon can be seen in Fig. 8. An advanced optical extensometer with the proportional gauge length which can be customized by the user was used to capture the full engineering stress-strain relationship. The original gauge length of the optical extensometer was determined based on the distance between the white dot customized by the customer. To have better consistency and for the purpose of easier comparison, the gauge length was approximately derived as 25 mm and 50 mm where elongation at fracture either 25 mm ($\varepsilon_{f,25}$) or 50 mm ($\varepsilon_{f,50}$) can be directly obtained from the video extensometer by laser beam. Meanwhile, the fine lines were marked along the parallel gauge side in case the fracture occurs outside the region of the video extensometer, which was determined by carefully fitting the fractured pieces and comparing the final gauge length to the original gauge length. Two linear electrical strain gauges were adhered to the mid-length on each side of a coupon and the averaged strain measurements were used to obtain the modulus of elasticity (E_s). During each tensile coupon test, the loading was paused near the yield and ultimate strengths for 90s for stress relaxation to obtain the static stress-strain curve by which the 0.2% proof stress ($f_{0.2}$) [21, 22], static ultimate tensile strength (f_u), the measured 0.05% proof stress ($f_{0.05}$), the strain hardening component for flat coupon plate n, the strain-hardening strain ε_{sh}, static ultimate tensile strain (ε_u) and elongation at fracture (ε_f) of the material can also be determined

4.1.2 Corner coupon tests

To examine the strength enhancement of the material properties of the corner portions caused by the press-braking process, the corner coupons were machined from the corner regions of specimens in CF1 and CF2 series. The width of the corner coupon is 4 mm along the gauge length to minimize the local eccentric load induced during the testing process. For each corner coupon, two holes with diameter of 10 mm were drilled at the distance of 20 mm from the end of the coupon. A pair of specially developed grips with two pins was utilized to apply the tensile load through its centroid [44], as depicted in Fig. 9. The tensile test procedures were identical to the flat coupon tests described in section 4.1.1. Typical stress-strain curves for corner coupons can be seen in Fig. 7 in comparison with those for flat coupons. Compared with the stress-strain relationship for the flat coupons, the underlying strength enhancements and the accompanied decrement of the ductility indicate the cold-forming effect on material properties caused by press-braking process, as evidenced in Fig. 10. For cold-formed sections associated with pronounced plastic deformation, the extracted coupon curved after removal from the section due to the release of the bending residual stresses through the thickness. No attempt was made to strengthen the coupon prior to tensile testing [14, 16].

4.1.3 Parent plate coupons

Virgin plate material properties are obtained by performing tensile coupon tests on specimens extracted from the parent plates. Six flat coupons were taken from each batch of the steel plate in the longitudinal and transverse directions. The electrical strain gauges were affixed to the mid-length on both sides of each coupon specimen to derive the Poisson's ratio v with which two were mounted longitudinally and the other two in transverse direction. The averaged material properties results from the measurements for the parent steel plates are summarized in Table 10 and Table 11, where $E_{s,p}$ indicate the elastic modulus of the parent steel plate, $f_{y,p}$ is yield strength, $f_{u,p}$ is the ultimate strength, $\varepsilon_{sh,p}$ is strain-hardening strain, $\varepsilon_{u,p}$ strain at ultimate strength, $\varepsilon_{f,p}$ (in case extensometer with different gauge length, subscript of 25 mm or 50 mm are accompanied with, eg. $\varepsilon_{f50,p}$ or $\varepsilon_{f25,p}$) elongation at fracture and $\varepsilon_{f,p}$ proportional elongation at fracture. The letter "p" in subscript indicates it is the material property from parent plate. Typical stress-strain curves of the parent plates are plotted in Fig. 11.

4.1.4 Tensile coupon specimens to examine strength variations within the cross section

The differences in material properties between the flat coupon and the corner coupon from the HSS hexagonal sections demonstrate the heterogeneous mechanical characteristics across the cross-sections which are affected by different fabrication routes. Therefore, to investigate the variation of the material properties within the cross section of HSS hexagonal sections, coupon specimens were extracted at different locations over one sixth or quarter of the cross-section and tested, as shown in Figs. 12-16. This arrangement was based on the symmetrical properties of the fabrication routes such as the symmetrical distribution of cold-bended corners or welding seams. To investigate the effect of the welding on the material properties, the tensile coupons were also machined from the welding seams and a coupon at a distance of 10 mm away from the welding seam was also extracted to study the effect of the welding on properties of materials close to the HAZ. The remaining coupons were taken accordingly within the section in flat and corner portions to investigate the variation of the material properties, where the corresponding extracted location are depicted in Figs. 12-16. The one-sixth section coupons and quarter section coupons were machined with 4 mm and 8 mm width for the plate with thickness of 6 mm and 10 mm respectively. The distribution and the magnitude of the yield strength and ultimate strength from the coupons within the section was plotted against the corresponding locations in Fig. 12 to Fig. 16. The measured material properties are summarized in Table 5-9.

Upon on completion of the comparison between the material properties between the welding seam and the flat coupon for W-series section, illustrative resemblance of the yield strength underpins the negligible effect of the welding on material properties in the vicinity of the welding seam, though the modulus of the coupon from the welding is softened and the ultimate strength are relatively higher. The negligible effect of the welding on the material properties near the welding seam may be principally attributed to the relatively narrow width of the HAZ and lower heat input by controlling the related parameters during welding. No effect of cooling rate on material properties have been found, where similar observations were also obtained [7]. Strength enhancements of 5.4%, 5.3%, 3.9% and 3.7% for 0.2% proof stress and 5.9%, 7.0%, 6.9% and 6.2% percent for ultimate strength compared with averaged properties from flat portion have been obtained for CF1-145 × 6, CF2-145 × 6, CF2-200 × 6 and CF2-145 × 10 sections respectively.

4.2 Estimation of strength enhancement at corners using existing models

The strength enhancement is observed for the coupon specimens machined from cold-formed sections, especially for the corner coupons taken from the regions where the relatively higher strain-hardening associated with pronounced plastic deformation was obtained, as depicted in Fig. 13 to Fig. 15. To effectively estimate the strain hardening effect, Karren [43] studied strength enhancement in the corners of the cold-formed steel sections with the use of the power model in terms of the yield strength of the undeformed parent steel. The area of the enhanced corner can account for approximate 5% to 30% area of the total cross-sectional area. The model for predicting the strength increment is given as Eq. (2) to Eq. (4) and the model is adopted in the current international design code for the Design of Cold-formed Steel Structural Members, AISI S100-16 [44].

$$f_{y,c} = \frac{B_c}{(r_i / t)^{\alpha}} f_y \tag{2}$$

where,

$$B_c = 3.69(\frac{f_u}{f_y}) - 0.819(\frac{f_u}{f_y})^2 - 1.79 \tag{3}$$

$$\alpha = 0.192(\frac{f_u}{f_y}) - 0.068 \tag{4}$$

t is thickness of the steel sheet, r_i is the inner radius, f_y is the yield strength of the steel material and $f_{y,c}$ is the enhanced yield strength at corner region.

Nevertheless, these equations are applicable to the structures with the bent angles lower than 120° and the ratio of the inner corner bent radius to thickness less than 7. Though the strength enhancement was provided in EN 1993-1-3, it was only applicable to the cold-formed section with 90 – degree corners. Hence, the suitability of the Eq. (2) to Eq. (4) for HSS hexagonal sections was assessed based on the experimental results of material properties obtained in this study.

In addition, based on this model, Pham et al. [45] extended it to high strength G450 cold-formed steel with nominal yield strength of 450 MPa. To overcome the inconsistent predicted results using the equations from AISI S100-16 [44], modifications were made and the suggested model to predict the enhanced strength of the corner regions for high strength G450 cold-formed steel are given as follows,

$$B_c = 1.588(\frac{f_u}{f_y}) - 0.281(\frac{f_u}{f_y})^2 - 0.038 \quad (5)$$

$$\alpha = 0.228(\frac{f_u}{f_y}) - 0.068 \quad (6)$$

In addition, the modified predictions for the enhanced strength of the corner coupon specimens taking into account the enhancement of the region adjacent to the corner region was provided by Gardner et al. [14] based on cold-formed box sections. The revised value for the coefficient was given in Eqs. (7) and (8). The effect of the cold-forming effect on the strength enhancement has been studied extensively and compared with numerous specifications in [119]. Likewise, these predictive models for quantifying the strength enhancements at corner regions were assessed based on the obtained results, as presented in Table 12. Based on the assessments, less accurate predictions were observed from the model provided by Pham et al. [45]. However, scattered results were found in the Table 12 indicating the need to develop improved corner strength enhancement models for HSS hexagonal hollow sections.

$$B_c = 2.9(\frac{f_u}{f_y}) - 0.752(\frac{f_u}{f_y})^2 - 1.09 \quad (7)$$

$$\alpha = 0.23(\frac{f_u}{f_y}) - 0.041 \quad (8)$$

4.3 Material models

An accurate material model for predicting the stress-strain relationship of the material plays vital importance to the structural design and analysis for the HSS hexagonal hollow section structures. Hence, the material model suitable for the development of stress-strain curves for HSS hexagonal hollow sections is required. The existing stress-strain models for hot-rolled steel with yield plateau and for cold-formed steel with relatively gradual stress-strain relationship after the stresses larger than the proportional limits are introduced in the subsequent sections. Based on the principles of the existing models, new stress-strain models for HSS hexagonal hollow sections were proposed and validated.

4.3.1 Hot-rolled material model

Hot-rolled steel, generally featured with a sharply defined yield point following the linear elastic range, present pronounced strain hardening after moderate development of the strain entering the yield plateau. To further improve the perfectly-plastic material models in EN 1993-1-1 [47] and ANSI/AISC 360-10 [48], efforts have consistently made to improve the accuracy particularly focusing on the strain hardening stage to avert overly-conservative prediction or unduly neglect of stiffness increasing. Quad-linear material model was proposed by Boeraeve et al. [49] and further revised by Yun and Gardner [50]. To trace the gradual loss of the stiffness, power model was proposed, as shown in Eq. (9),

$$\sigma \begin{cases} E_s \varepsilon & for\ \varepsilon \le \varepsilon_y \\ f_y & for\ \varepsilon_y \le \varepsilon \le \varepsilon_{sh} \\ f_y + (f_u - f_y)[0.4\varepsilon_x + 2\varepsilon_x / (1+400\varepsilon_x{}^5)^{\frac{1}{5}}] & for\ \varepsilon_{sh} \le \varepsilon \le \varepsilon_u \end{cases} \quad (9)$$

where ε_x is equal to $(\varepsilon-\varepsilon_{sh})/(\varepsilon_u-\varepsilon_{sh})$.

It should be noted that hardening strain ε_{sh} generally is not provided in the mill certificates and it can be calculated using Eqs. (10) and (11) generated through regression analysis

$$\varepsilon_{sh} = 0.1\frac{f_y}{f_u} - 0.055 \qquad for \quad 0.015 \le \varepsilon_{sh} \le 0.03 \quad (10)$$

$$\varepsilon_u = 0.6(1 - \frac{f_y}{f_u}) \qquad for \quad \varepsilon_{sh} \ge 0.06 \quad (11)$$

4.3.2 Stress-strain model for materials in cold-formed sections

Cold-formed steel sections can undergo severe plastic deformation leading to a more rounded response of the stress-strain relationship compared with hot-rolled steel, particularly for the cold-bent corner with smaller corner radius thickness ratio indicating relatively large plastic strain associated with the press-braking process. The Ramberg-Osgood relationship is widely adopted as the basic form for developing the full range stress-strain relationship for cold-formed steel sections [50-53].

$$\varepsilon = \frac{\sigma}{E_s} + 0.002(\frac{\sigma}{f_y})^n \quad (12)$$

To accurately represent the curve up to the ultimate strength without overly predicting the yield strength, Gardner and Yun [54] derived a model based on collected test results for steel stress-strain curves aiming at developing material models applicable for cold-formed carbon steel precisely and the model is given in Eq. (13) to Eq. (15).

$$\varepsilon = \begin{cases} \dfrac{\sigma}{E_s} + 0.002\left(\dfrac{\sigma}{f_{0.2}}\right)^n & for \quad \sigma \le f_{0.2} \\ \dfrac{\sigma - f_{0.2}}{E_{0.2}} + \left(\varepsilon_u - \varepsilon_{0.2} - \dfrac{f_u - f_{0.2}}{E_{0.2}}\right)\left(\dfrac{\sigma - f_{0.2}}{f_u - f_{0.2}}\right)^m + \varepsilon_{0.2} & for \ \sigma > f_{0.2} \end{cases} \tag{13}$$

where

$$m = 1 + 3.3(\frac{f_{0.2}}{f_u}) \tag{14}$$

$$E_{0.2} = \frac{E_s}{1 + 0.002nE_s / f_{0.2}} \tag{15}$$

or alternatively obtained from the following with the 1.0% proof stress needed,

$$m = \frac{\ln(0.008 + \dfrac{\sigma_{1.0} - f_y}{E} - \dfrac{\sigma_{1.0} - f_y}{E_{0.2}}) - \ln(\varepsilon_u - \varepsilon_{0.2} - \dfrac{f_u - f_y}{E_{0.2}})}{\ln(\sigma_{1.0} - f_y) - \ln(f_u - f_y)} \tag{16}$$

In terms of the determination of the first-stage strain hardening parameters *n*, Rasmussen and Hancock [53], Arrayago et al. [54] and Gardner and Yun [55] concluded that with 0.05% proof stress instead of 0.01% proof stress yields more consistent values. Thus, the first stage hardening component n is determined as follows,

$$n = \frac{\ln(4)}{\ln(f_y / \sigma_{0.05})} \tag{17}$$

In addition to the model introduced above, a material stress-strain model for HSS cold-formed sections is proposed by Ma et al. [5] by relating the strain hardening component to plastic strain ε_p. The strain hardening component can be obtained based on Eq. (18). In the equation, *m* and *K* are the coefficients used to determine the proportional increment of strain hardening exponent n_{pro}. Coefficient *K* can be calculated using Eq. (20), and the exponent m is determined by fitting the model to the tested stress-strain curve.

$$n_{pro} = f(\varepsilon_p) = n + K\varepsilon_p{}^m \quad (18)$$

$$\varepsilon_p = \varepsilon - \frac{\sigma}{E} = 0.002(\frac{\sigma}{f_{0.2}})^{n_{pro}} \quad (19)$$

$$K = [\log_{\frac{f_u}{f_{0.2}}}(\frac{\varepsilon_u - f_u / E_s}{0.002})] / (\varepsilon_u - f_u / E_s)^m \quad (20)$$

Substituting Eq. (18) into Eq. (19), the expression of Eq. (21) can be obtained as follows, by which the predicted strength and the stress-strain correlated well with the experimental stress-strain curve.

$$\begin{cases} \sigma = \left(\dfrac{\varepsilon_{\mathrm{p}}}{0.002}\right)^{\left(\frac{1}{n+K\varepsilon_{\mathrm{p}}^{m}}\right)} f_{0.2} \\ \varepsilon = \varepsilon_{\mathrm{p}} + \dfrac{\sigma}{E_{\mathrm{s}}} = \varepsilon_{\mathrm{p}} + \dfrac{f_{0.2}}{E_{\mathrm{s}}}\left(\dfrac{\varepsilon_{\mathrm{p}}}{0.002}\right)^{\left(\frac{1}{n+K\varepsilon_{\mathrm{p}}^{m}}\right)} \end{cases} \quad (21)$$

4.3.3 Proposed stress-strain model for HSS hexagonal sections

Based on the obtained results from the coupon tests for HSS hexagonal hollow sections, it is noted that stress-strain relationship features both with plateau and relatively rounded stress-strain response were included in these three series HSS hexagonal hollow sections. Hence, the stress-strain models are proposed for these two distict stess-strain relationships. Concerning the stress-strain relationship with yield plateu, non-linear strain hardening range markably resembles the initial part of Ramberg-Osgood model up to 0.2% proof strength. A modified Ramberg-Osgood model to describe the stress-strain behaviour of the non-linear strain-hardening range is proposed for Q690 steel with certain level of non-linear strain hardening. Commencing from the strain-hardening point, the stress-strain relationship can be expressed by Eq. (22)

$$\varepsilon - \varepsilon_{\mathrm{sh}} = \frac{\sigma - f_{\mathrm{y}}}{E_{\mathrm{sh}}} + \left(\varepsilon_{\mathrm{u}} - \varepsilon_{\mathrm{sh}} - \frac{f_{\mathrm{u}} - f_{\mathrm{y}}}{E_{\mathrm{sh}}}\right)\left(\frac{\sigma - f_{\mathrm{y}}}{f_{\mathrm{u}} - f_{\mathrm{y}}}\right)^{m^*} \quad (22)$$

$$(1)\ \text{Bilinear: } \sigma = \begin{cases} E_s\varepsilon & \text{for } \varepsilon \le \varepsilon_y \\ f_y & \text{for } \varepsilon_y < \varepsilon \le \varepsilon_{sh} \end{cases}$$
$$(2)\ \text{nonlinear: } \varepsilon = \varepsilon_{sh} + \frac{\sigma - f_y}{E_{sh}} + \left(\varepsilon_u - \varepsilon_{sh} - \frac{f_u - f_y}{E_{sh}}\right)\left(\frac{\sigma - f_y}{f_u - f_y}\right)^{m*} \quad \text{for } \sigma > f_y \tag{23}$$

in which m^* is the strain-hardening exponent, E_{sh} is the initial slope of the stress-strain curves in the strain-hardening range, also termed as hardening modulus. E_{sh} can be directly obtained from material tests. If the value is not reported, Eq. (24) proposed in Yun and Gardner [49] might be used to determine the value.

$$E_{sh} = \frac{f_u - f_y}{0.4(\varepsilon_u - \varepsilon_{sh})} \tag{24}$$

Since the characteristics of stress-strain properties of HSS are different from those for conventuonal strength steel, the equations for estimating paramters in the model need to be developped. The modified equations for ε_u *and* ε_{sh} are proposed in Eqs. (25) and (26) based on the material properties database collected for Q690 steel and the tensile coupon tests results obtained in this study, as shown in Fig. 17 and Fig. 18. The collated database is summarized in Table 13.

$$\varepsilon_{sh} = -0.04\frac{f_y}{f_u} + 0.06 \quad \textit{for} \quad 0.01 \le \varepsilon_{sh} \le 0.04 \tag{25}$$

$$\varepsilon_u = 0.55(1 - \frac{f_y}{f_u}) + 0.03 \tag{26}$$

Moreover, it is found that the second stage hardening parameter *m* accounting for accurate prediction for the stage of strain hardening can be utilized to describe the initial hardening parameter in the first stage before strain hardening after transformation, which provide relatively accurate prediction, as depicted in Fig. 19. Hence, the expression of *m* in Eq. (14) was adopted for initial stage prediction in the proposed model.

Concerning the stress-strain relationship for the materials with relatively rounded shape, material model describing cold-formed steel proposed in [5] and [54] was assessed firstly. The comparisons of the stress-strain curves between the tests results and the predicted curves are depicted in Fig. 19 and Fig. 20. The predictions from model proposed by Gardner and Yun [54] overestimate the stress-strain response after the yield point whereas the model proposed by Ma et al. [5] and the proposed cold-formed model with modified parameters offer better predictions. However, the derivations from the model provided by Ma et al. [5] need repeated iterations and the expressions is lengthy, it is suggested to use the proposed model to obtain the rounded stress-strain relationship for HSS hexagonal cold-formed steel hollow sections. It was found that more accurate result can be obtained by replacing the first stage limit point $f_{0.2}$ with $f_{0.5}$ and the parameter m can be taken as 2 which provided the most accurate predictions. Hence, to formulate relatively accurate stress-strain response, further investigations were needed to develop the second stage hardening parameter m based on larger database for high strength steel with rounded responses.

5. Residual stresses investigation

Residual stresses, considered as an initial state existing in structures prior to the externally applied loading are caused by various manufacture processes such as cold-formed process (i) press-braking; (ii) cold-rolled process; (iii) coiling and uncoiling of the steel sheet etc. and welding that induces uneven cooling/heating, as thermal-type stresses. Residual stresses can adversely affect the structural behaviour since they can cause premature yielding through part of the material thickness, leading to the further loss of the stiffness of the structure due to its superimposed stresse, and reduced stability and bearing capacity of the structural members [5, 19, 21, 22, 56].
Residual stresses can distribute in different directions for structures. Longitudinal and transverse directions are the two main categories and the residual stresses in the longitudinal direction are more influential than those in the transverse direction, as illustrated by Ziemian [56] and Schafer et al. [57]. Hence, this study focused on longitudinal residual stresses which can be further de-composed into membrane residual stresses and bending residual stresses, as represented in Fig. 21. The methods for measuring residual stresses are mainly classified as destructive method and non-destructive method. Non-destructive methods include X-ray diffraction method, neutron or electron diffraction method, ultrasonic method and magnetic methods, whereas destructive methods are generally referred to the sectioning method and hole drilling method. Sectioning method is a widely used destructive method based on the measurements of the deformations of the material before and after being extracted from the structural members. This method has been successfully applied in previous studies [59, 60] for residual stress measurements and thus was also adopted for this study.

5.1 Residual stresses measurement procedures

The residual stresses measurements were also conducted for the HSS hexagonal hollow sections considered for material properties measurements. The length of the specimens for the measurements was 400 mm. Due to the symmetry of geometrical properties of hexagonal hollow sections for this study, a quarter section of each specimen was marked into longitudinal strips with width varying between 10 mm, 12 mm and 15 mm, depending on the residual stress gradient and distribution. Strain gauges of model FLAB-5-11-1LJC-F and adhesive of model CN of Tokyo Sokki Kenkyujo are adopted with a 5 mm gauge length which allows reliable and accurate measurements of strains up to 5%, were mounted onto the outer and inner surfaces of the longitudinal strips at mid-height of each strip. The waterproof tape was subsequently applied to cover each electrical strain gauge to avoid damaging during the cutting process. The external and internal views of the specimen CF2-145 × 6 are presented in Fig. 22. Both external and internal initial strain gauge readings were taken prior to the sectioning. The wire cutting method was employed to perform the sectioning with coolant sprayed to minimize the heat generated during the sectioning process, as shown in Fig. 23. Typical deformed strips extracted from CF2-145 × 6 after sectioning are depicted in Fig. 24. After the completion of the sectioning process, the released residual stresses induced by manufacturing process were taken on the basis of the readings from strain gauges. For readings from each strain gauge, at least three times readings were taken and the mean value was used for subsequent analysis. The residual strains on the outer and inner surfaces of each longitudinal strips were measured based on the differences between the strain before and after the sectioning process, by which subtracting the initial strain readings from the final readings, the residual strains can be determined. Moreover, the membrane and bending residual strains can be determined from Eq. (27) and Eq. (28) after which the residual stresses can be derived on the basis of the simple Hook's Law.

$$\sigma_m = -(\frac{\varepsilon_{ext} + \varepsilon_{int}}{2})E_s = (\frac{\varepsilon_{ext,f} - \varepsilon_{ext,i}}{2} + \frac{\varepsilon_{int,f} - \varepsilon_{int,i}}{2})E_s \quad (27)$$

$$\sigma_b = -(\frac{\varepsilon_{ext} - \varepsilon_{int}}{2})E_s = (\frac{\varepsilon_{ext,f} - \varepsilon_{ext,i}}{2} - \frac{\varepsilon_{int,f} - \varepsilon_{int,i}}{2})E_s \quad (28)$$

5.2 Results and discussion

The magnitude and the distribution of the longitudinal residual stresses in W-145 × 6, CF1-145 × 6, CF2-145 × 6, CF2-200 × 6 and CF2-145 × 10 were determined. The membrane and bending residual stresses for the W-145 × 6 section were firstly determined on the basis of the assumption that the bending residual stresses vary linearly through the thickness [19, 60] of the welded sections. It should be noted that the positive and negative value indicate the tensile and compressive residual stresses respectively. The magnitude and the distribution of the calculated membrane and bending residual stresses for W-145 × 6 section are presented in Fig. 25, in which the maximum membrane and bending residual stresses are marked. The obtained residual stresses are also normalized by the yield strength of parent plate and plotted with respect to the distance from the welding seam. As can be seen in Fig. 25, membrane residual stresses for the W-145 × 6 section are much larger than the bending residual stresses. The largest membrane residual stresses were observed at the welding seam and surrounding areas while gradually decreased and changed to compressive membrane stresses when the distance from welding is becoming larger. Compressive bending residual stresses are observed along the external surface of the one-sixth section. The largest tensile membrane residual stress for W-145 × 6 is 45% of the $f_{0.2,p}$ whereas the largest compressive membrane residual stress is 18.5% of the $f_{0.2,p}$. Furthermore, bending residual stresses ranged between 4.8 and 16.7% of the yield strength of parent plate.

The distribution and magnitude of residual stresses for the sections CF1-145 × 6, CF2-145 × 6, CF2-200 × 6 and CF2-145 × 10 fabricated with combined process of welding and press braking were also estimated and characterized. The calculated membrane and bending residual stresses for each section are presented in Fig. 26 to Fig. 29. The extracted strips from the sections in CF1 and CF2 series were observed with larger curvature deformation in comparison with strips taken from W-series, as result of the large bending residual stresses due to the associated excessively strain hardening and pronounced plastic deformation experienced during press-braking process. The bending residual stresses are much larger at the corner than any other regions, as observed from Fig. 26 to Fig. 29. The maximum tensile bending residual stresses in CF1-145 × 6, CF2-145 × 6, CF2-200 × 6 and CF2-145 × 10 sections respectively were 27.3, 30.9, 35.3 and 42.7% of the $f_{0.2,p}$ of the parent plate. In terms of membrane residual stresses, maximum tensile membrane residual stresses are found at the welding seam and became relatively small at other regions. The maximum membrane residual stresses are invariably larger than the bending residual stresses. It is found that the maximum membrane residual stresses for CF1-145 × 6, CF2-145 × 6, CF2-200 × 6 and CF2-145 × 10 were 43, 65, 51 and 62% of the $f_{0.2,p}$ of the parent plate. After comprehensively comparing the magnitude and distribution of the membrane and residual stresses for section of W-145 × 6, CF1-145 × 6, CF2-145 × 6, the different patterns existed in these three sections further demonstrate the effect of the fabrication routes on residual stresses should be accounted for in the analysis.

5.3 Proposed model for residual stress distribution

The test results of the residual stresses measurement were subsequently utilized for the development of the predictive membrane and bending residual stress models for HSS hexagonal hollow sections. Incorporating these models in numerical analysis will allow for accurate predictions for structural behaviour. To have relative easier applications, multi-linear model was adopted as simplified distribution of residual stress with constant value at corner regions, as depicted in Fig. 30 to Fig. 32. The magnitudes of the residual stresses given in the models were obtained as the average membrane and bending residual stresses over different locations of the hollow sections and the distribution models were plotted with respect to one-sixth and quarter sections with normalized values against parent plate yield strength $f_{0.2,p}$.

Constant tensile and compressive bending residual stresses at specific locations were given since the variation of bending residual stresses at these locations were lower in comparison with membrane residual stresses. Weng and White [63] and Moen et al. [64] have observed that the residual stresses are related to the ratio of bending radius to thickness. Hence, bending residual stress for sections with fabrication route CF2 should be similar since they are featured with same r/t ratio equal to 3. Nevertheless, the residual stress in compact section CF2-145 × 10 with thicker plate featured with relatively higher bending residual stresses than CF2-145 × 6 which may principally attribute to the higher level of strain-hardening, indicating that the bending residual stresses magnitude is related to the thickness as well other than r/t ratio.

6. Conclusions

The material properties and residual stress distribution in HSS hexagonal hollow sections produced with three fabrication routes have been experimentally investigated in this study. A total of 76 tensile coupons were taken from the HSS hexagonal hollow sections and the parent steel plates. The material properties were found to be insensitive to the welding in the sections formed by welding six plates. For the sections fabricated with press-braking processes, strength enhancements were observed for the coupons taken from the corner portion with 0.2% proof stress and ultimate tensile strength up to 5.5% and 7.6% respectively, due to the cold-working of the press-braking process. The applicability of the predictive model for strength enhancement at corner was assessed and modified based on the obtained test results. A new material model to describe the stress-strain relationship for the flat portion with yield plateau was developed which can yield satisfactory prediction in the stage of strain-hardening and the existing stress-strain model for cold-formed steel was modified and applied to the corner materials achieving good agreements with test results. The distribution and the magnitudes of the residual stresses were experimentally investigated and the largest membrane and bending residual stresses were found to be up to 62% and 42.7% of the material yield strength. In terms of the bending residual stresses, magnitudes at the corner were much higher than those of at the flat portion while the largest membrane residual stresses were found near the welding seam. A predictive model for distribution and the magnitude of the residual stresses in HSS hexagonal hollow sections were proposed based on the test results.

Acknowledgements

The research work presented in this paper was supported by a grant from the Research Grants Council of the Hong Kong Special Administrative Region, China (Project no. 152189/18E). The authors would like to sincerely acknowledge the support from the Innovation and Technology Fund - Nano and Advanced Materials Institute (ITF-NAMI) for the project “Hong Kong Modular Integrated Construction (MiC) Innovations” (PolyU/ ZS12) and from the Chinese National Engineering Research Centre for Steel Construction (Hong Kong Branch) at The Hong Kong Polytechnic University. The authors would also like to thank the technical staff, Mr. H.Y. Leung, Mr. K.L. Cheung and Mr. F.H. Wong, of the Structural Engineering Research Laboratory. The support from Industrial Center was also acknowledged.

References

[1] T.M. Chan, X.L. Zhao, B. Young, Cross-section classification for cold-formed and built-up high strength carbon and stainless steel tubes under compression, J. Constr. Steel. Res. 106 (2015) 289-295.

[2] J.Y. Zhu, T.M. Chan, B. Young, Cross-sectional capacity of octagonal tubular steel stub columns under uniaxial compression, Eng. Struc. 184 (2019) 480-494.

[3] J. Wardenier, J. Packer, X.L. Zhao, G. Van der Vegte, Hollow sections in structural applications, Bouwen met staal

Rotterdam,, The Netherlands, 2002.
[4] N. Baddoo, A.Q. Chen, High strength steel design and execution guide. The Steel Construction Institute, Silwood Park, Ascot, Berkshire, UK. 2020
[5] J.L. Ma, T.M. Chan, B. Young, Material properties and residual stresses of cold-formed high strength steel hollow sections, J. Constr. Steel. Res. 109 (2015) 152-165.
[6] S. Nie, Q. Zhu, B. Yang, P. Li, Investigation of residual stresses in Q460GJ steel plates from medium-walled box sections, J. Constr. Steel. Res. 148 (2018) 728-740.
[7] H. Fang, T.M. Chan, B. Young, Behavior of Octagonal High-Strength Steel Tubular Stub Columns, J. Struct. Eng. 145 (2019)
[8] W. Xu, L.H. Han, W. Li, Performance of hexagonal CFST members under axial compression and bending, J. Constr. Steel. Res. 123 (2016) 162-175.
[9] T. Aoki, Y. Migita, Y. Fukumoto, Local buckling strength of closed polygon folded section columns, J. Constr. Steel. Res. 20 (1991) 259-270.
[10] Y. Migita, T. Aoki, Y. Fukumoto, Local and interaction buckling of polygonal section steel columns, J. Struct. Eng. 118 (1992) 2659-2676.
[11] B. Evirgen, A. Tuncan, K. Taskin, Structural behavior of concrete filled steel tubular sections (CFT/CFSt) under axial compression, Thin-Walled Struct. 80 (2014) 46-56.
[12] T. Reinke, P. Knoedel, T. Ummenhofer, Steel poles with polygonal sections in bending, European Conference on Steel and Composite Structures, Naples, Italy, 2014,
[13] J.Y. Zhu, T.M. Chan, Behaviour of polygonal-shaped steel-tube columns filled with high-strength concrete, Proc. Inst. Civil Eng.-Struct. Build. 171 (2018) 96-112.
[14] L. Gardner, N. Saari, F. Wang, Comparative experimental study of hot-rolled and cold-formed rectangular hollow sections, Thin-Walled Struct. 48 (2010) 495-507.
[15] W.W. Yu, R.A. LaBoube, H. Chen, Cold-formed steel design, Wiley Online Library, 2010.
[16] M. Sun, J.A. Packer, Direct-formed and continuous-formed rectangular hollow sections — Comparison of static properties, J. Constr. Steel. Res. 92 (2014) 67-78.
[17] T.J. Li, G.Q. Li, Y.B. Wang, Residual stress tests of welded Q690 high-strength steel box-and H-sections, J. Constr. Steel. Res. 115 (2015) 283-289.
[18] A. Paradowska, J.W. Price, R. Ibrahim, T. Finlayson, A neutron diffraction study of residual stress due to welding, J. Mater. Process. Technol. 164 (2005) 1099-1105.
[19] R.B. Cruise, L. Gardner, Strength enhancements induced during cold forming of stainless steel sections, J. Constr. Steel. Res. 64 (2008) 1310-1316.
[20] B. Rossi, S. Afshan, L. Gardner, Strength enhancements in cold-formed structural sections—Part II: Predictive models, J. Constr. Steel. Res. 83 (2013) 189-196.
[21] H. Fang, T.M. Chan, B. Young, Material properties and residual stresses of octagonal high strength steel hollow sections, J. Constr. Steel. Res. 148 (2018) 479-490.
[22] J.B. Chen, H.X. Liu, T.M. Chan, Material properties and residual stresses of cold-formed octagonal hollow sections, J. Constr. Steel. Res. 170 (2020)
[23] K. Tayyebi, M. Sun, Stub column behaviour of heat-treated and galvanized RHS manufactured by different methods, J. Constr. Steel. Res. 166 (2020) 105910.
[24] P.Y. Cheng, Influence of residual stress and heat affected zone on fatigue failure of welded piping joints, (2009)
[25] K. Sefcikova, T. Brtnik, J. Dolejs, K. Keltamaki, R. Topilla, Mechanical properties of heat affected zone of high strength

steels, IOP Conference Series: Materials Science and Engineering, 96, 2015, 012053
[26] F. Wang, O. Zhao, B. Young, Testing and numerical modelling of S960 ultra-high strength steel angle and channel section stub columns, Eng. Struc. 204 (2020) 109902.
[27] AWS A5.28/A5.28M, Specification for Low-Alloy Steel Electrodes and Rods for Gas Shielded Arc Welding, American Welding Society, United States of America, 2005.
[28] D. Stemne, T. Narström, B. Hrnjez, Welding Handbook: A guide to better welding of Hardox and Weldox, SSAB, 2010.
[29] ASTM E94, Standard Guide for Radiographic Examination, American Society for Testing and Materials, 2000.
[30] Z. Yan, H. Xu, P. Huang, Multi-scale multi-intensity defect detection in ray image of weld bead, NDT & E International. 116 (2020) 102342.
[31] GB 50205, Standard for acceptance of construction quality of steel structures, China Architecture & Building Press, Beijing, China, 2020.
[32] GB/T-3323, Non-destructive testing of welds-Radiographic testing - Part 1: X- and gamma -ray techniques with film, Standards Press of China, Qinhuangdao, China, 2019.
[33] ISO 17636-2, Non-destructive testing of welds — Radiographic testing — Part 2: X- and gamma-ray techniques with digital detectors, International Organization for Standardization, 2013.
[34] GB 50661, Code for welding of steel structures, China Architecture & Building Press, Beijing, China, 2011.
[35] ASTM E 2002, Standard Practice for Determining Total Image Unsharpness and Basic Spatial Resolution in Radiography and Radioscopy, American Society for Testing and Materials, 2015.
[36] K. Goebbels, Surface crack detection by magnetic particle inspection, NDT International. 30 (1988) 327-332.
[37] F.P.G. Márquez, A.M.P. Chacón, A review of non-destructive testing on wind turbines blades, Renew. Energy. (2020)
[38] EN ISO 6892-1, Metallic Materials – Tensile Testing Part 1: Method of Test at Ambient Temperature, CEN, Brussels, Belgium, 2019.
[39] R. Bjorhovde, Development and use of high performance steel, J. Constr. Steel. Res. 60 (2004) 393-400.
[40] B. Karabulut, B. Rossi, On the fatigue behavior of duplex and high-strength welded cruciform joints, Eng. Struc. 247 (2021) 113161.
[41] H. Ho, K. Chung, X. Liu, M. Xiao, D. Nethercot, Modelling tensile tests on high strength S690 steel materials undergoing large deformations, Eng. Struc. 192 (2019) 305-322.
[42] Y. Huang, B. Young, Structural performance of cold-formed lean duplex stainless steel columns, Thin-Walled Struct. 83 (2014) 59-69.
[43] K.W. Karren, Corner properties of cold-formed steel shapes, J. Struct. Div. 93 (1967) 401-432.
[44] AISI S100-16, North American Specification for the Design of Cold-Formed Steel Structural Members, AISI (American Iron and Steel Institute), Washington, DC, USA, 2016.
[45] C.H. Pham, H.N. Trinh, G. Proust, Effect of manufacturing process on microstructures and mechanical properties, and design of cold-formed G450 steel channels, Thin-Walled Struct. 162 (2021) 107620.
[46] EN 1993-1-1, Eurocode 3: Design of Steel STRUCTURES – Part 1.1: General Rules and Rules for Buildings, European Committee for Standardization (CEN), Brussels, 2005.
[47] ANSI/AISC 360-16, Specification for Structural Steel Buildings, American Institute of Steel Construction (AISC), Chicago, 2016.
[48] P. Boeraeve, B. Lognard, J. Janss, J. Gerardy, J. Schleich, Elasto-plastic behaviour of steel frame works, J. Constr. Steel. Res. 27 (1993) 3-21.
[49] X. Yun, L. Gardner, Stress-strain curves for hot-rolled steels, J. Constr. Steel. Res. 133 (2017) 36-46.
[50] W. Ramberg, W.R. Osgood, Description of stress-strain curves by three parameters, (1943)

[51] H. Hill, Determination of stress-strain relations from" offset" yield strength values, 1944.
[52] K. Rasmussen, G. Hancock, Design of cold-formed stainless steel tubular members. II: Beams, J. Struct. Eng. 119 (1993) 2368-2386.
[53] W. Quach, J.G. Teng, K.F. Chung, Three-stage full-range stress-strain model for stainless steels, J. Struct. Eng. 134 (2008) 1518-1527.
[54] L. Gardner, X. Yun, Description of stress-strain curves for cold-formed steels, Constr. Build. Mater. 189 (2018) 527-538.
[55] I. Arrayago, E. Real, L. Gardner, Description of stress-strain curves for stainless steel alloys, Mater. Des. 87 (2015) 540–552。
[56] R.D. Ziemian, Guide to stability design criteria for metal structures, John Wiley & Sons, 2010.
[57] B.W. Schafer, Z. Li, C.D. Moen, Computational modeling of cold-formed steel, Thin-Walled Struct. 48 (2010) 752-762.
[58] M.T. Chen, B. Young, Material properties and structural behavior of cold-formed steel elliptical hollow section stub columns, Thin-Walled Struct. 134 (2019) 111-126.
[59] J. Chen, T.M. Chan, Material properties and residual stresses of cold-formed high-strength-steel circular hollow sections, J. Constr. Steel. Res. 170 (2020) 106099.
[60] P.J. Withers, H. Bhadeshia, Residual stress. Part 1–measurement techniques, Mater. Sci. Technol. 17 (2001) 355-365.
[61] A. Díaz, I. Cuesta, J. Alegre, A. de Jesus, J. Manso, Residual stresses in cold-formed steel members: review of measurement methods and numerical modelling, Thin-Walled Struct. 159 (2021) 107335.
[62] C. Weng, R. White, Residual stresses in cold-bent thick steel plates, J. Struct. Eng. 116 (1990) 24-39.
[63] C.D. Moen, T. Igusa, B.W. Schafer, Prediction of residual stresses and strains in cold-formed steel members, Thin-Walled Struct. 46 (2008) 1274-1289.
[64] J.F. McDermott, Plastic Bending of A514 Steel Beams, J. Struct. Div. 95 (1969) 1851-1187
[65] K.J.R. Rasmussen, G.J. Hancock, Plate slenderness limits for high strength steel sections, J. Constr. Steel. Res. 23 (1992) 73-96.
[66] B. Yuan, Local buckling of high strength steel W-shaped sections, Master, Ontario, Canada, McMaster University, 1997.
[67] E.S. Salem, R. Sause, Flexural strength and ductility of highway bridge I-girders fabricated from HPS-100W steel, ATLSS Reports, 2004,
[68] R.B. Tang, Plate yield slenderness criteria for structural members fabricated from high strength steels, Doctoral, Ph.D. Brisbane, Australia, Queensland University of Technology, 2008.
[69] A.M.G. Coelho, F.S.K. Bijlaard, H. Kolstein, Experimental behaviour of high-strength steel web shear panels, Eng. Struc., (2009) 1543-1555.
[70] G. Shi, H.Y. Ban, F.S.K. Bijlaard, Y.J. Shi, Y.Q. Wang, Experimental study and finite element analysis on the overall buckling behavior of ultra-high strength steel compression members with end restraints, China Civil Engineering Journal. 44 (2011) 17-25. (in Chinese)
[71] J.B. Yan, J.Y.R. Liew, M.H. Zhang, J.Y. Wang, Mechanical properties of normal strength mild steel and high strength steel S690 in low temperature relevant to Arctic environment, Materials and Design. 61 (2014) 150-159. (in Chinese).
[72] J.Y. Xue, Experimental research on the overall buckling behavior of high strength steel members under compression, Master, Nanjing, China, Southeast University, 2014. (in Chinese).
[73] S.P. Chiew, M.S. Zhao, C.K. Lee, Mechanical properties of heat-treated high strength steel under fire/ post-fire conditions, J. Constr. Steel. Res. 98 (2014) 12-19.
[74] S.W. Chen, X. Chen, Y.B. Wang, Z.L. Lu, G.Q. Li, Experimental and numerical investigations of Q690D H-section columns under lateral cyclic loading, J. Constr. Steel. Res. 121 (2016) 268-281.
[75] T.J. Li, S.W. Liu, G.-Q. Li, S.-L. Chan, Y.-B. Wang, Behavior of Q690 high-strength steel columns: Part 2: Parametric

study and design recommendations, J. Constr. Steel. Res. 122 (2016) 379-394.

[76] J. Wang, L. Gardner, Flexural Buckling of Hot-Finished High-Strength Steel SHS and RHS Columns, J. Struct. Eng. 143 (2017)

[77] Y.B. Wang, G.Q. Li, X. Sun, S.W. Chen, L.T. Hai, Evaluation and prediction of cyclic response of Q690D steel, Proceedings of the Institution of Civil Engineers-Structures and Buildings, 170(SB11),, 2017, 788-803

[78] T.Y. Ma, Y.F. Hu, X. Liu, G.Q. Li, K.F. Chung, Experimental investigation into high strength Q690 steel welded H-sections under combined compression and bending, J. Constr. Steel. Res. 138 (2017) 449-462.

[79] Y. Zhang, Overall stability behaivor of Q690GJ welded H-shaped section beams, M.Sc. Nanjing, China, Southeast University, 2017. (in Chinses).

[80] L.P. Hao, Experimental study on static and fatigue property of high strength steel welded joints, Master, M.Sc. Xi'an, China, Xi'an University of Technology, 2017. (in Chinese)

[81] X. Liu, Structural effects of welding onto high strength S690 steel plates and welded sections, (2017)

[82] Q. Peng, Investigation of flexural resistance and rotation capacity in Q690 high strength steel welded H-shaped flexural members, Master, M.Sc. Nanjing, China, Southeast University, 2018. (in Chinese).

[83] L.T. Hai, F.F. Sun, C. Zhao, G.Q. Li, Y.B. Wang, Experimental cyclic behavior and constitutive modeling of high strength structural steels, Constr. Build. Mater. 189 (2018) 1264-1285.

[84] K. Wang, Study on structural behaviour of high strength steel S690 welded H-and I-sections, Doctoral, Ph.D. thesis. Hong Kong, Civil and environmental engineering, Hong Kong Polytechnic University, 2018.

[85] L. Huang, G.Q. Li, X.X. Wang, C. Zhang, L. Choe, M. Engelhardt, High temperature mechanical properties of high strength structural steels Q550, Q690 and Q890, Fire Technol. 54 (2018) 1609-1628.

[86] H. Ho, X. Liu, K.F. Chung, A. Elghazouli, M. Xiao, Hysteretic behaviour of high strength S690 steel materials under low cycle high strain tests, Eng. Struc. 165 (2018) 222-236.

[87] Q. Sun, S. Qu, X. Wu, Ultimate load capacity analysis of Q690 high-strength steel KK-type tube–gusset plate connections, J. Struct. Eng. 145 (2019) 04019074.

[88] Z. Huang, D. Li, B. Uy, H.-T. Thai, C. Hou, Local and post-local buckling of fabricated high-strength steel and composite columns, J. Constr. Steel. Res. 154 (2019) 235-249.

[89]B. Lai, J.Y. Richard Liew, T. Wang, Buckling behaviour of high strength concrete encased steel composite columns, J. Constr. Steel. Res. 154 (2019) 27-42.

[90]Y. Sun, Y. Liang, O. Zhao, Testing, numerical modelling and design of S690 high strength steel welded I-section stub columns, J. Constr. Steel. Res. 159 (2019) 521-533.

[91] M. Amraei, S. Afkhami, V. Javaheri, J. Larkiola, T. Skriko, T. Björk, X.L. Zhao, Mechanical properties and microstructural evaluation of the heat-affected zone in ultra-high strength steels, Thin-Walled Struct. 157 (2020) 107072.

[92] L.L. Zhang, F.Y. Wang, Y.T. Liang, O. Zhao, Press-braked S690 high strength steel equal-leg angle and plain channel section stub columns: Testing, numerical simulation and design, Eng. Struc. 201 (2019) 109764

[93] T. Le, M.A. Bradford, X. Liu, H.R. Valipour, Buckling of welded high-strength steel I-beams, J. Constr. Steel. Res. 168 (2020) 105938.

[94] Y. Guo, H. Ho, K. Chung, A. Elghazouli, Cyclic deformation characteristics of S355 and S690 steels under different loading protocols, Eng. Struc. 221 (2020) 111093.

[95] A. Su, Y. Sun, Y. Liang, O. Zhao, Material properties and membrane residual stresses of S690 high strength steel welded I-sections after exposure to elevated temperatures, Thin-Walled Struct. 152 (2020) 106723.

[96] H. Ho, M. Xiao, Y. Hu, Y. Guo, K. Chung, M. Yam, D. Nethercot, Determination of a full range constitutive model for high strength S690 steels, J. Constr. Steel. Res. 174 (2020), 106275

[97] Y.F. Hu, K.-F. Chung, H. Ban, D.A. Nethercot, Investigations into residual stresses in S690 cold-formed circular hollow sections due to transverse bending and longitudinal welding, Eng. Struc. 219 (2020) 110911

[98] C. Zhang, R. Wang, G. Song, Effects of pre-fatigue damage on mechanical properties of Q690 high-strength steel, Constr. Build. Mater. 252 (2020) 118845.

[99] E. Cadoni, D. Forni, Strain-rate effects on S690QL high strength steel under tensile loading, J. Constr. Steel. Res. 175 (2020) 106348.

[100] K.F. Chung, H.-C. Ho, Y.-f. Hu, K. Wang, X. Liu, M. Xiao, D.A. Nethercot, Experimental evidence on structural adequacy of high strength S690 steel welded joints with different heat input energy, Eng. Struc. 204 (2020) 110051.

[101] F. Wang, E.M. Lui, Experimental study of the post-fire mechanical properties of Q690 high strength steel, J. Constr. Steel. Res. 167 (2020) 105966.

[102] X.M. Lin, M.C. Yam, K.-F. Chung, A.C. Lam, A study of net-section resistance of high strength steel bolted connections, Thin-Walled Struct. 159 (2021) 107284.

[103] B. Yang, M. Dong, Q. Han, M. Elchalakani, G. Xiong, Flexural Behavior and Rotation Capacity of Welded I-Beams Made from 690-MPa High-Strength Steel, J. Struct. Eng. 147 (2021) 04020320.

[104] H. Bartsch, F. Eyben, G. Pauli, S. Schaffrath, M. Feldmann, Experimental and Numerical Investigations on the Rotation Capacity of High-Strength Steel Beams, J. Struct. Eng. 147 (2021) 04021067.

[105] EN 10219-2, Cold formed welded steel structural hollow sections. Tolerances, dimensions and sectional properties, European Committee for Standardization (CEN), Brussels, 2019.

[106] A500/A500 M, Standard Specification for Cold-Formed Welded and Seamless Carbon Steel Structural Tubing in Rounds and Shapes, American Society for Testing and Materials, 2021.

[107] A1085/1085M, Specification for Hollow Structural Sections (HSS), American Society for Testing and Materials, West Conshohocken, PA, USA, 2015.

[108] GB/T 6728, Cold forming hollow sectional steel for general structure, Standards Press of China, Beijing, China, 2017.

[109] AS/NZS 1163, Cold-formed structural steel hollow sections, Standards Australia, 2016.

[110] JIS G 3101, Rolled steels for general structure, Japanese Standards Association 2015.

[111] JIS G 3128: 2009(E): High Yield Strength Steel Plates for Welded Structure, JSA, Tokyo, Japan, 2009.

[112] JIS G 3466, Carbon steel square and rectangular tubes for general structure, Japanese Standards Association 2015.

[113] G40.20-13/G40.21, General requirements for rolled or welded structural quality steel / Structural quality steel, CSA, 2018.

[114] Strenx, Hardox and Docol , Bending of high strength steel., SSAB, 2017.

[115] ISO 14346, Static design procedure for welded hollow-section joints — Recommendations, International Organization for Standardization 2013.

[116] M. Amraei, A. Ahola, S. Afkhami, T. Björk, A. Heidarpour, X.L. Zhao, Effects of heat input on the mechanical properties of butt-welded high and ultra-high steels, Eng. Struc. 198 (2019) 109460."

[117] X. Liu, K.F. Chung, H.C. Ho, M. Xiao, Z.X. Hou, D. A. Nethercot, Mechanical behavior of high strength S690-QT steel welded sections with various heat input energy. Eng. Struc. 175 (2018) 109460." 245-256."

[118] EN 10025-6, Hot-rolled products of structural steels – Technical delivery conditions for flat products of high yield strength structural steels in the quenched and tempered condition, European Committee for Standardization (CEN), 2004.

[119] Z. Liu, H. Liu, Z. Chen, G. Zhang, Structural behavior of cold-formed thick-walled ctangular steel columns, J. Constr. Steel Res. 147 (2018) 277-292.

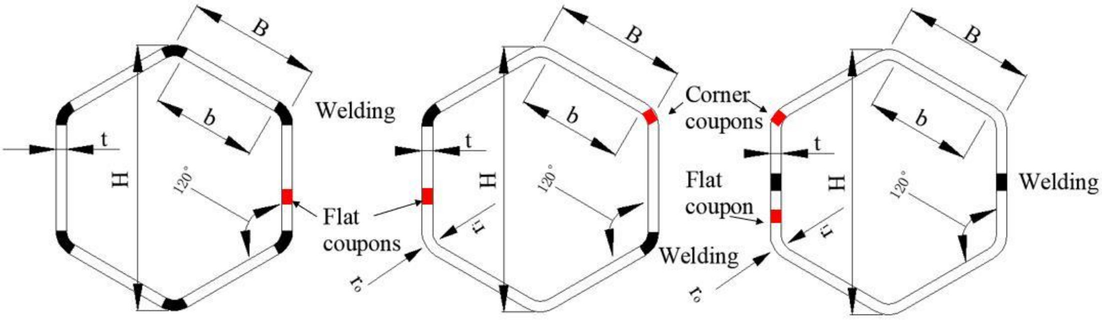

(a) W Series (b) CF1 Series (c) CF2 Series

Fig. 1 Cross sectional views of the examined regular hexagonal specimens

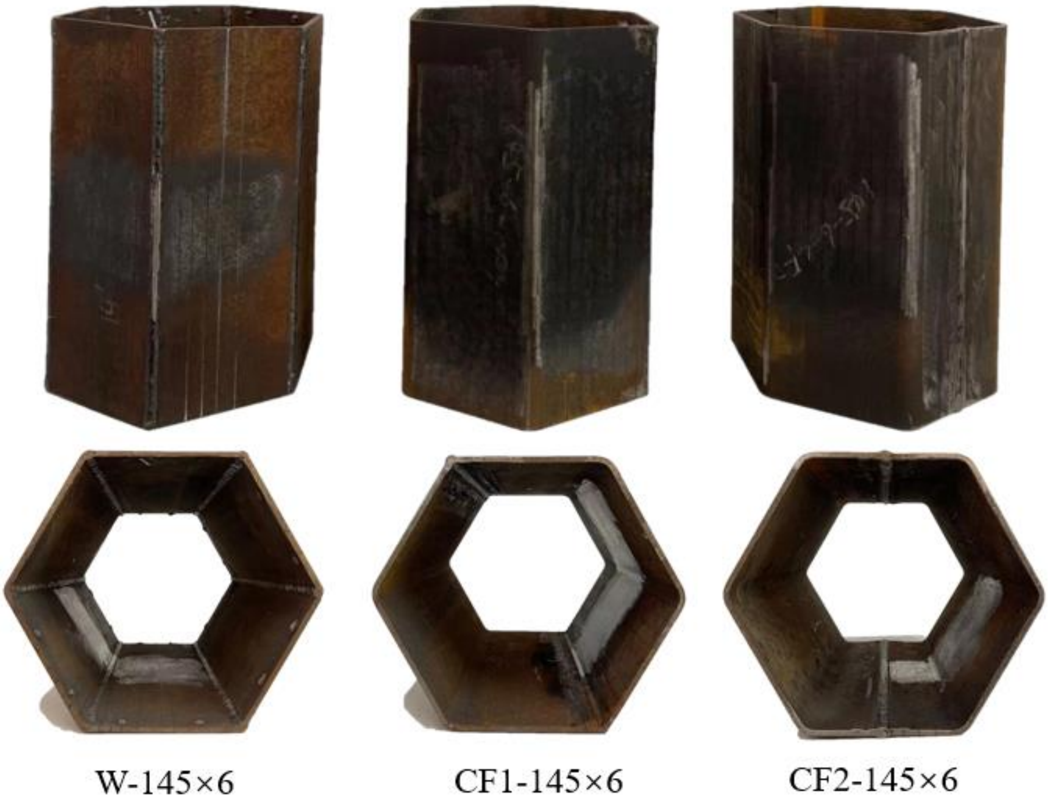

Fig. 2 Images of W-145×6, CF1-145×6 and CF2-145×6 specimens with three different fabrication routes investigated in this study.

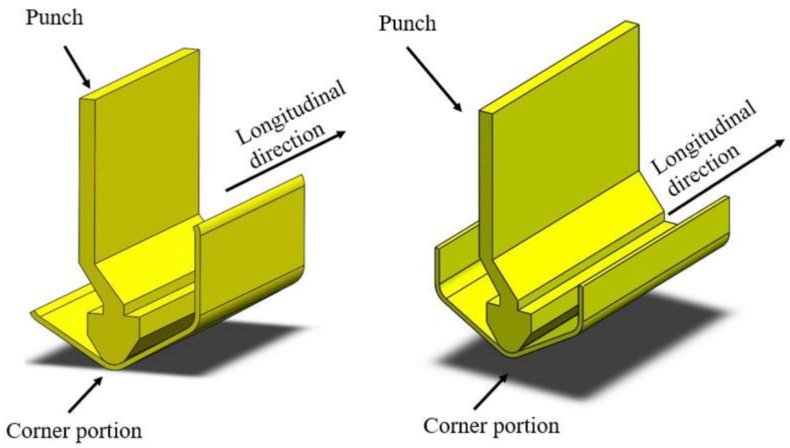

Fig. 3 Schematic view of the press-braking process for specimens in CF1 and CF2 series

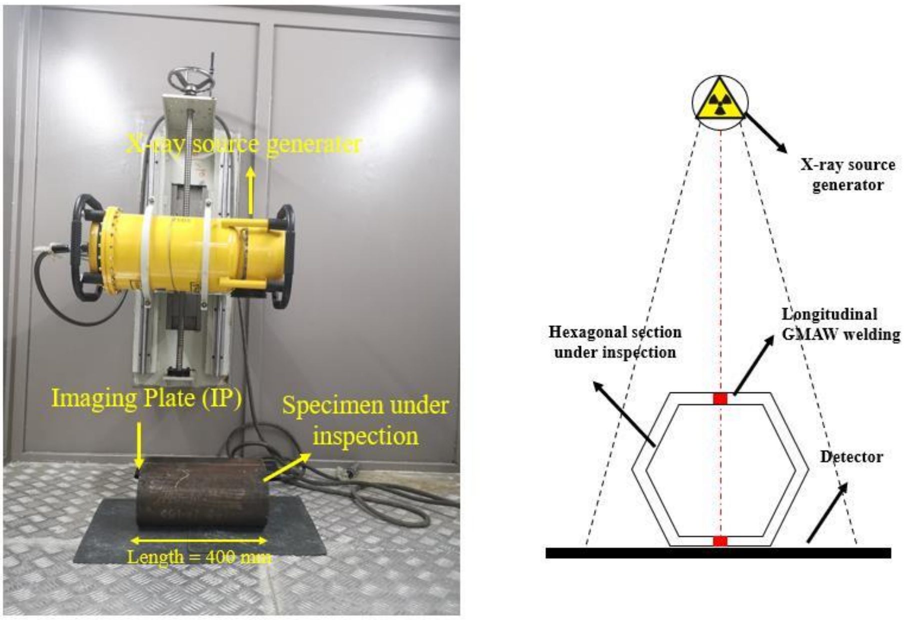

Fig. 4 Schematic view of the X-ray inspection method for welding inspection

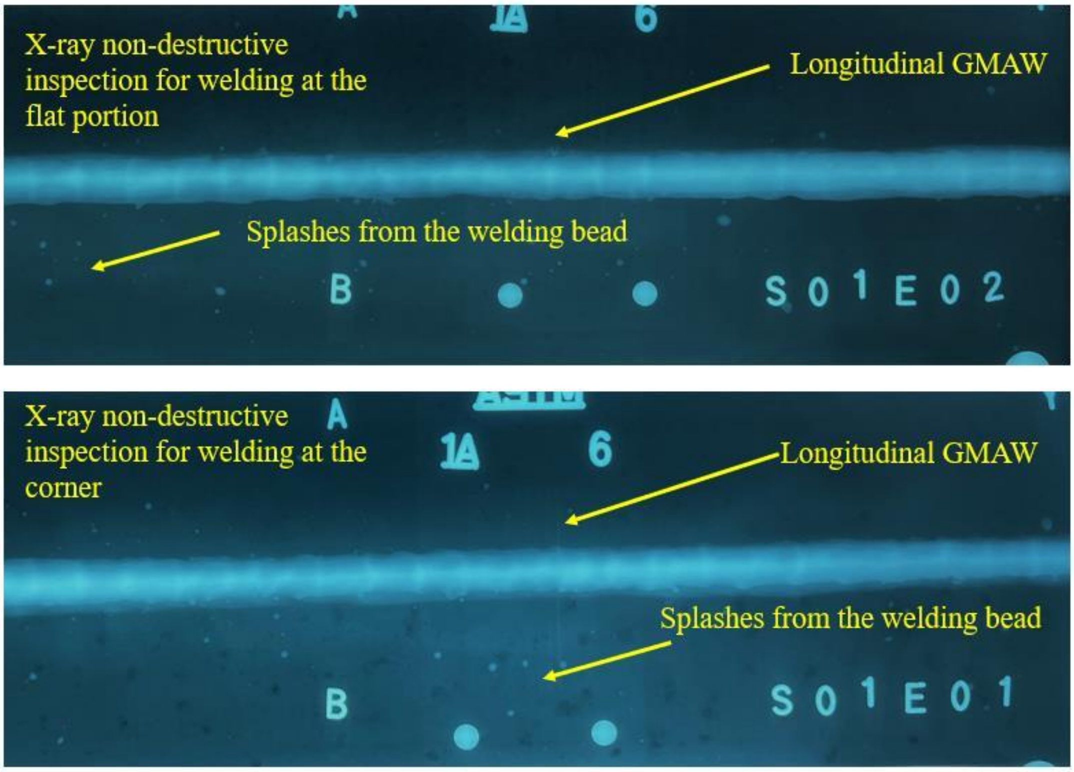

Fig. 5 X-ray non-destructive inspection for the corner welding and butt welding at flat portion

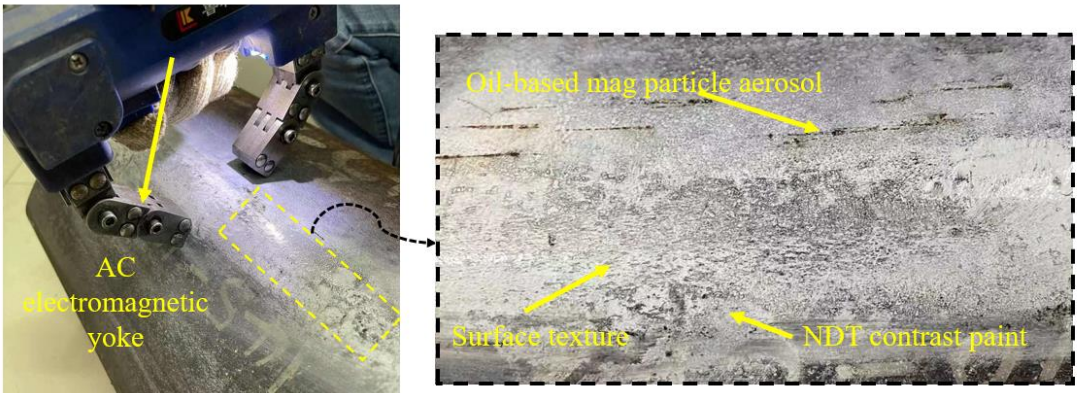

Fig. 6 Magnetic particle inspection method for surface crack detection

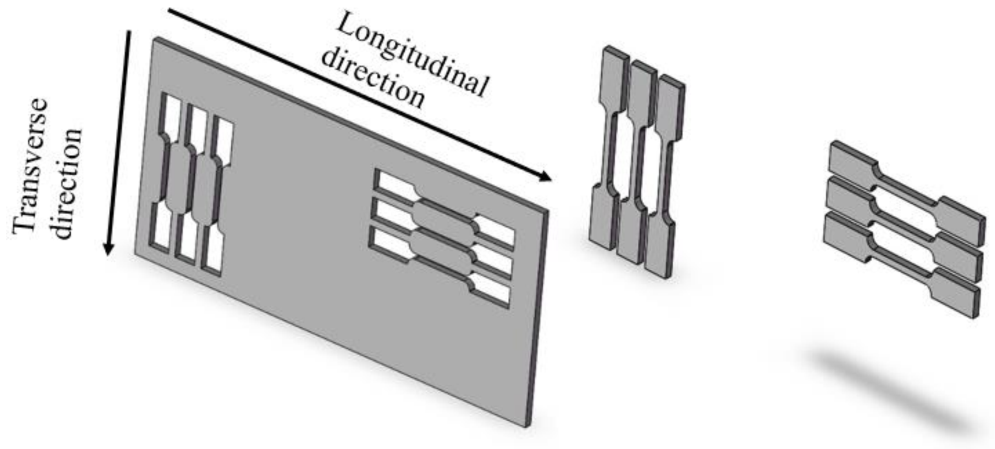

Fig. 7 Location of the coupons extracted from parent plate (both for 6 mm and 10 mm plates)

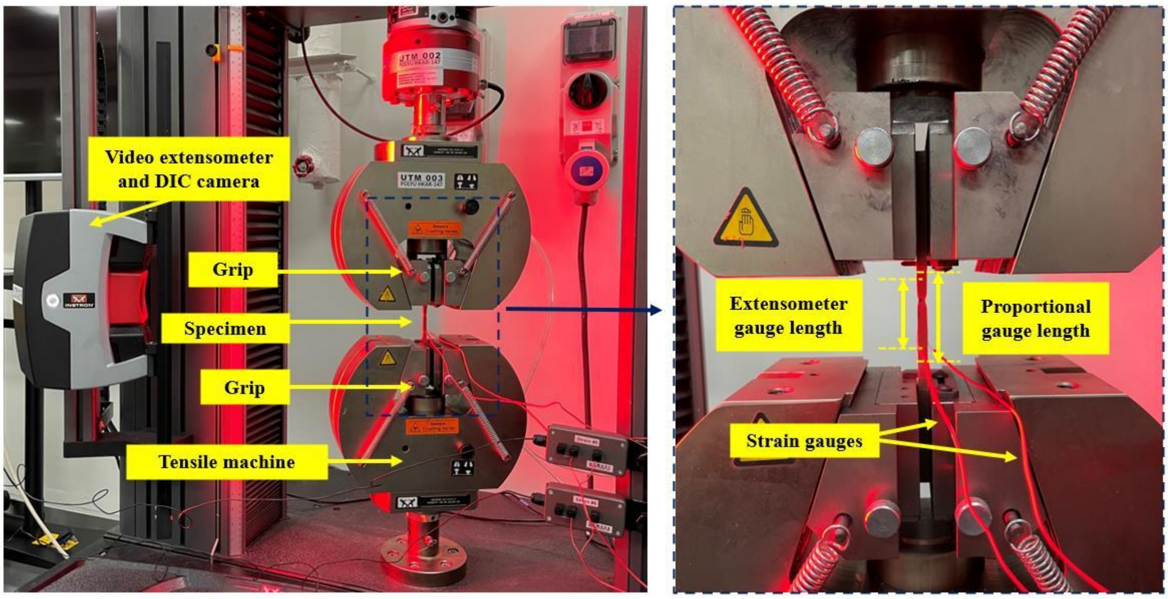

Fig. 8 Test arrangement of the flat and parental tensile coupons

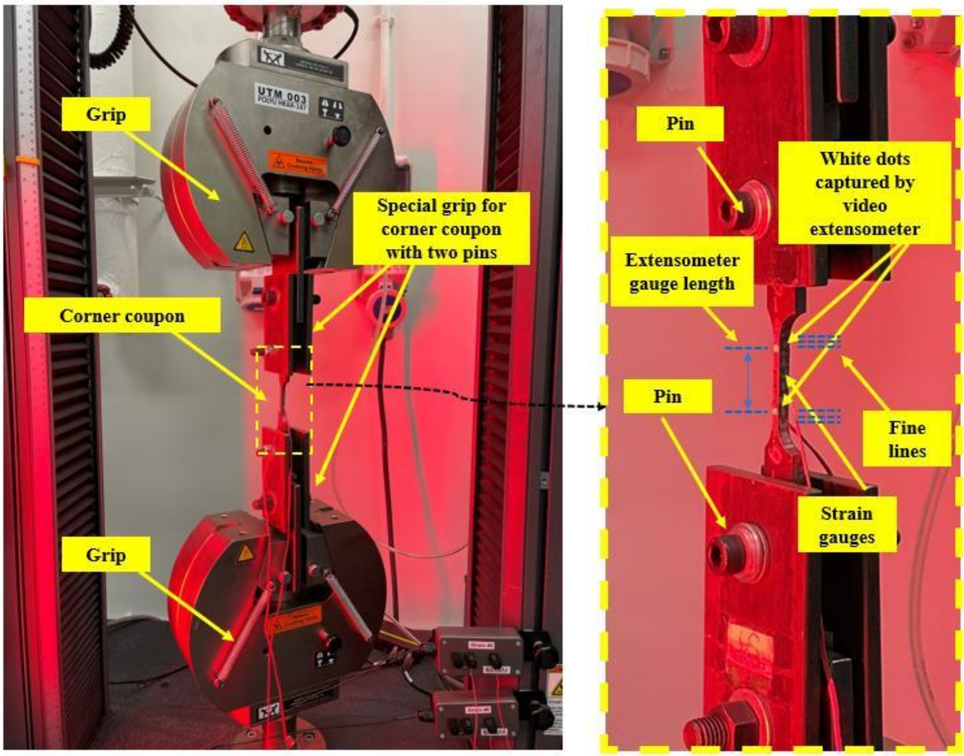

Fig. 9 Test arrangement for the corner coupons with a specimen in place

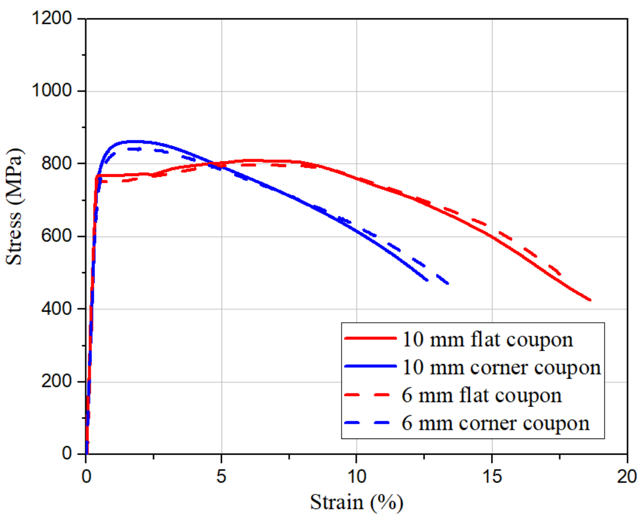

Fig. 10 Typical stress-strain curves of the tensile flat and corner coupons taken from HSS hexagonal hollow sections of CF1-145×6 and CF2-145×10

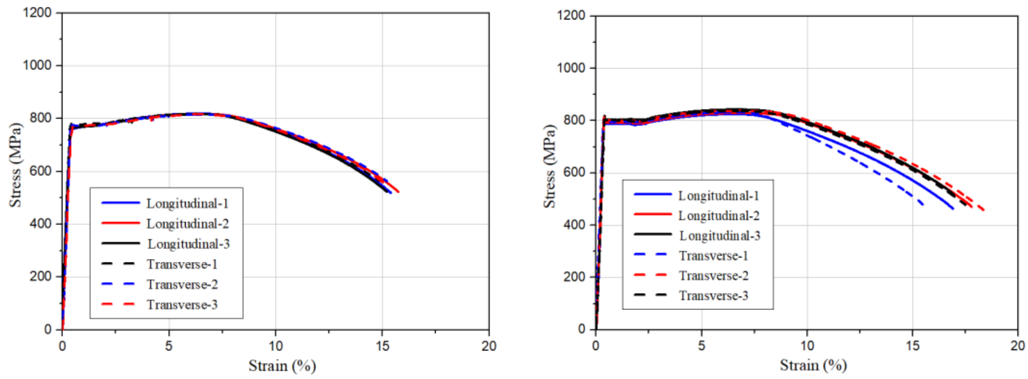

Fig. 11 Stress-strain curves of the coupon specimens taken from parent plates (a) 6 mm steel plate (b) 10 mm steel plate

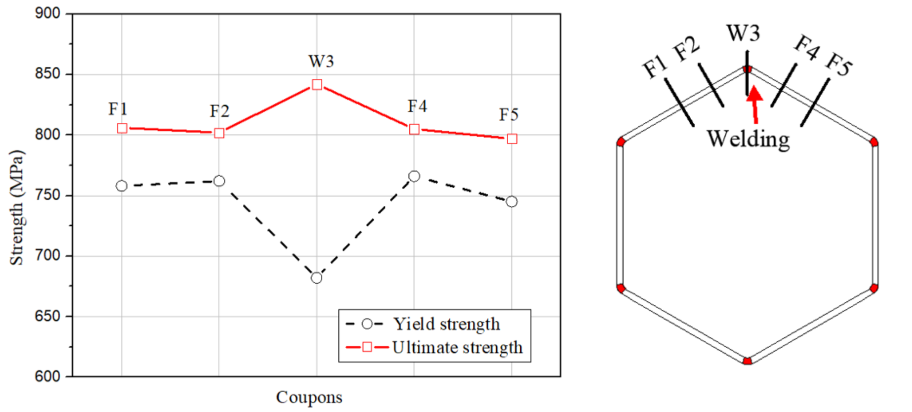

Fig. 12 Disribution of the yield strength and ultimate strength within the section HSS hexagonal W-145×6 sections

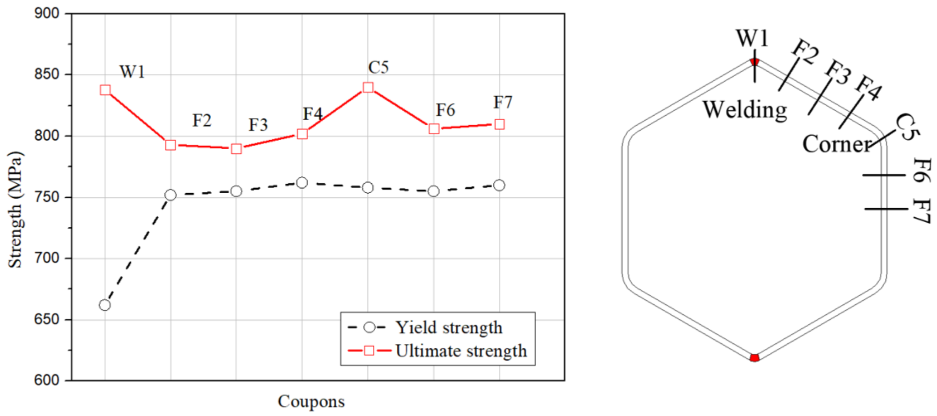

Fig. 13 Disribution of the yield strength and ultimate strength within the cross-section of HSS hexagonal CF1-145×6 sections

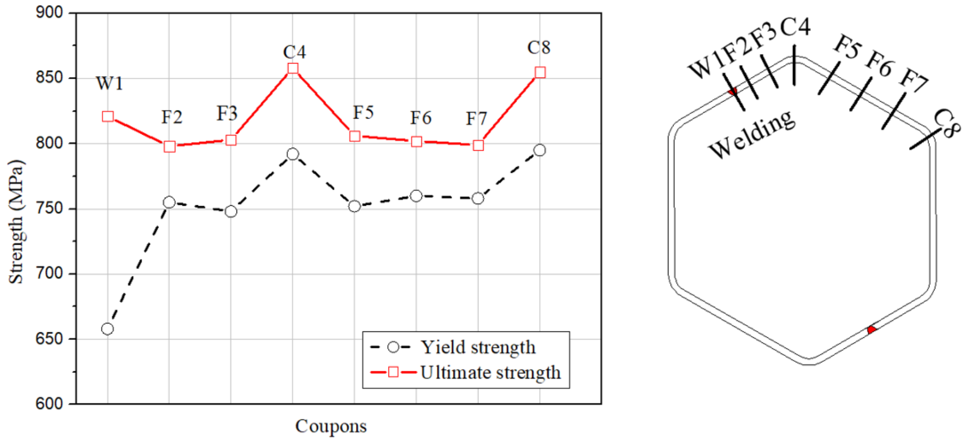

Fig. 14 Disribution of the yield strength and ultimate strength within the section HSS hexagonal CF2-145×6 sections

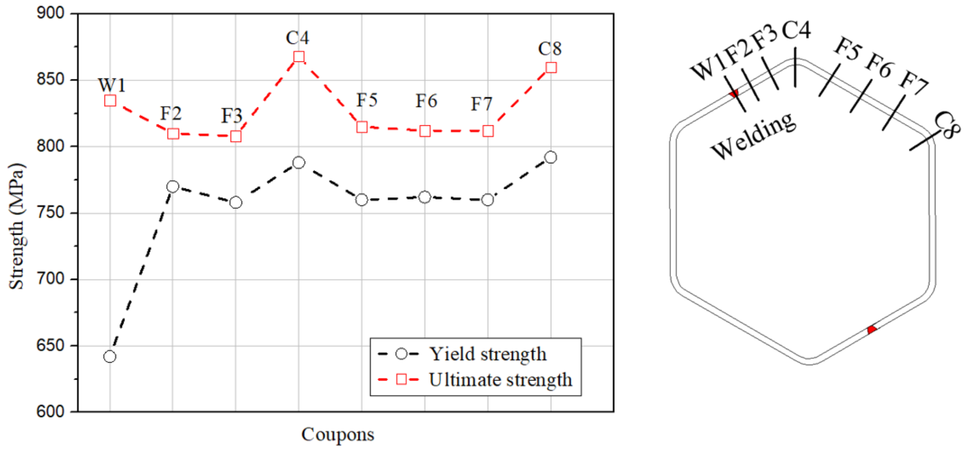

Fig. 15 Disribution of the yield strength and ultimate strength within the section HSS hexagonal CF2-200×6 sections

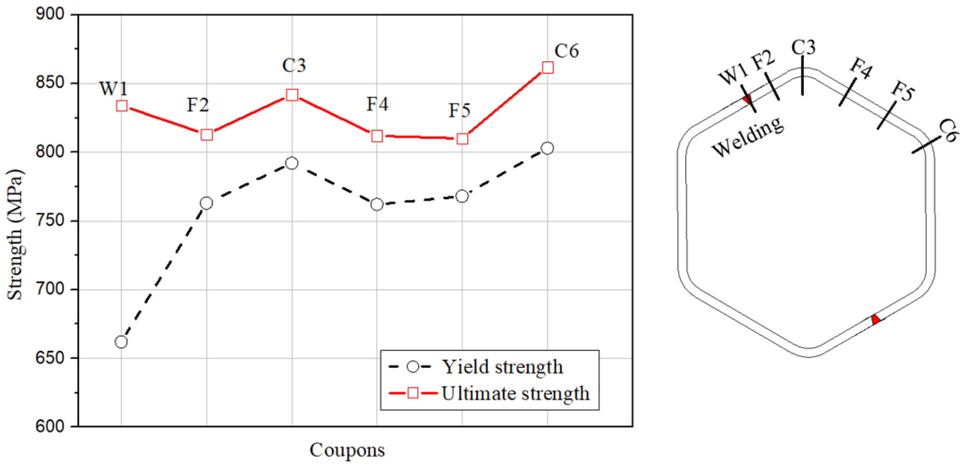

Fig. 16 Disribution of the yield strength and ultimate strength within the section HSS hexagonal sections CF2-145×10

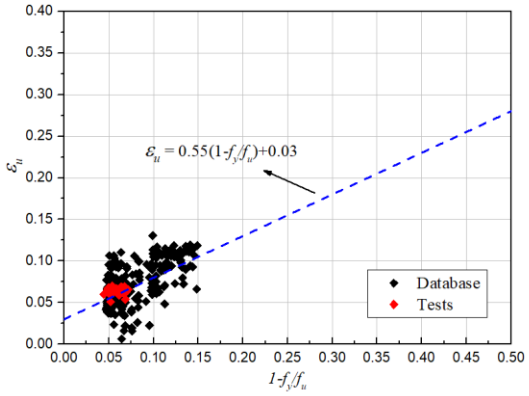

Fig. 17 Evaluation of predictive expression for Q690 steels

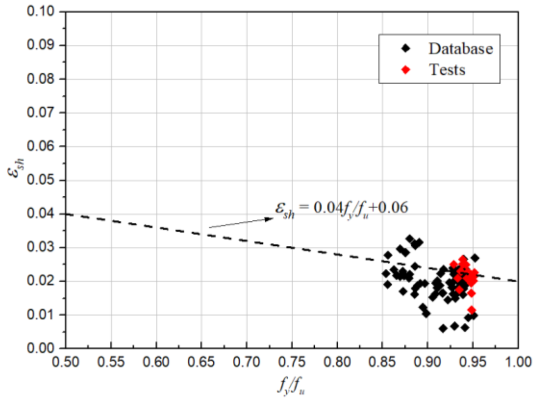

Fig. 18 Evaluation of predictive expression for Q690 steels with yield plateu

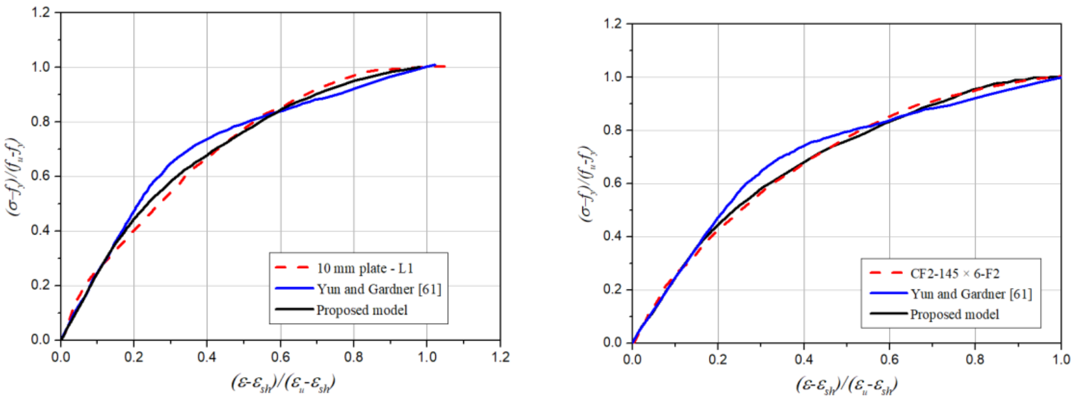

(a) Flat coupon from parent sheet of 10 mm (b) Flat coupon from cold-formed section

Fig. 19 Comparison of the proposed model with the flat coupon test results with yield plateau

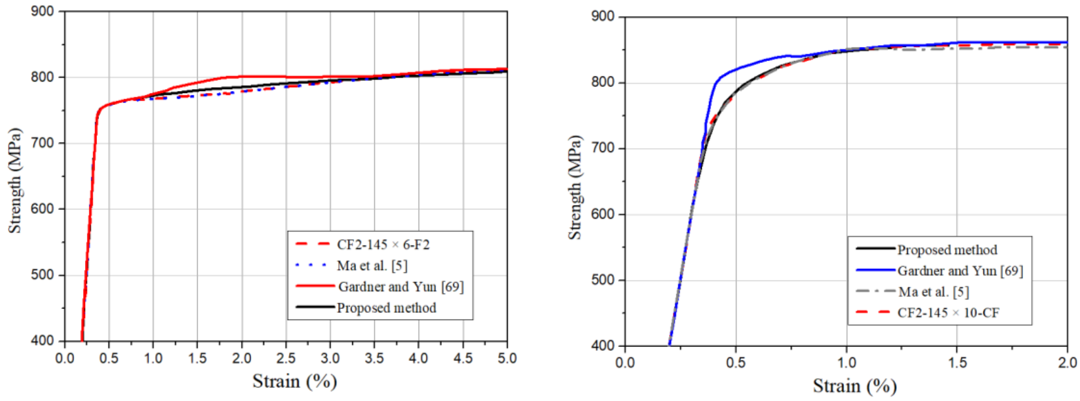

(a) Flat coupon from cold-formed Q690 steel (b) Corner coupon from cold-formed Q690 steel

Fig. 20 Comparison of the proposed model with the flat coupon and corner coupon test results with rounded responses

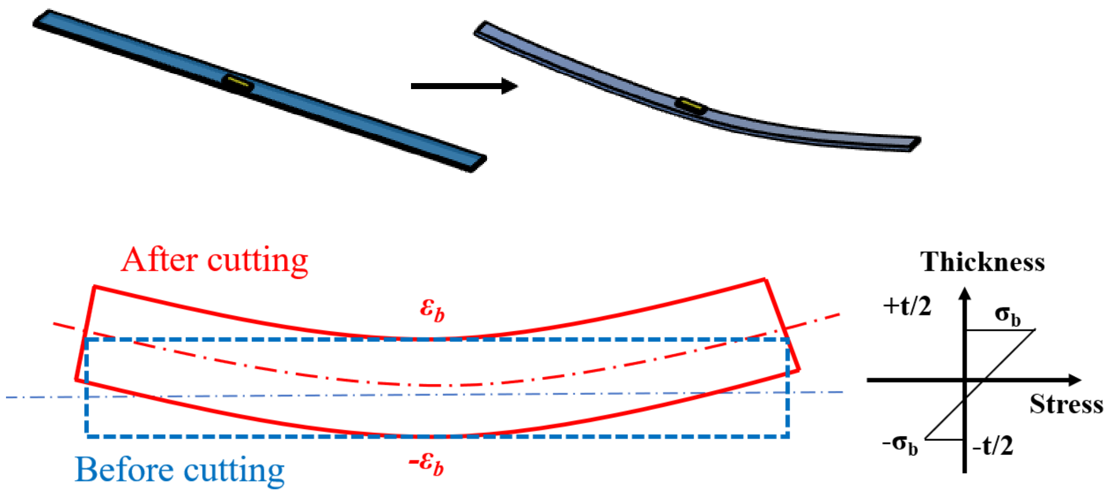

(a) Bending residual stress

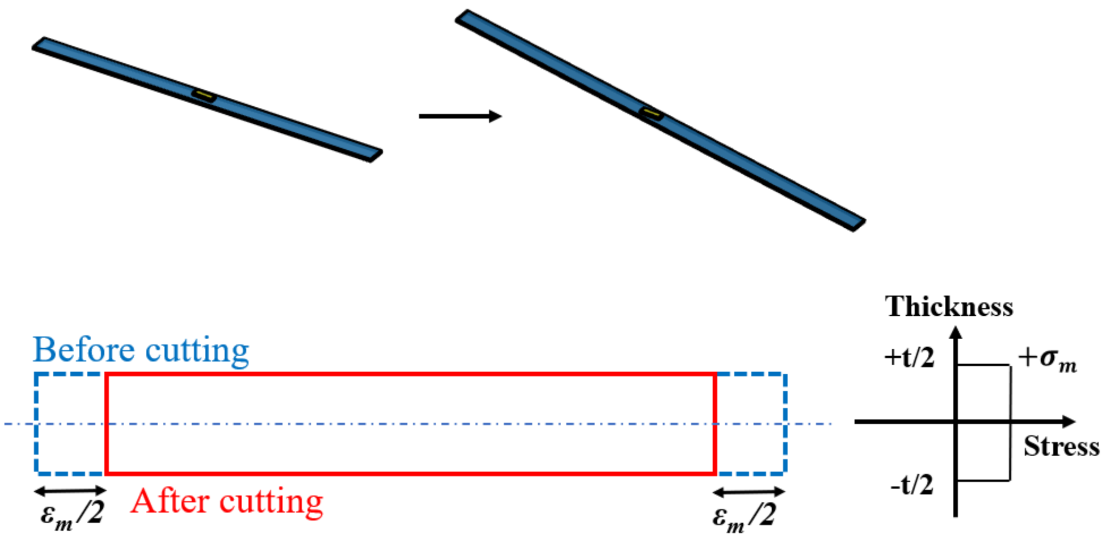

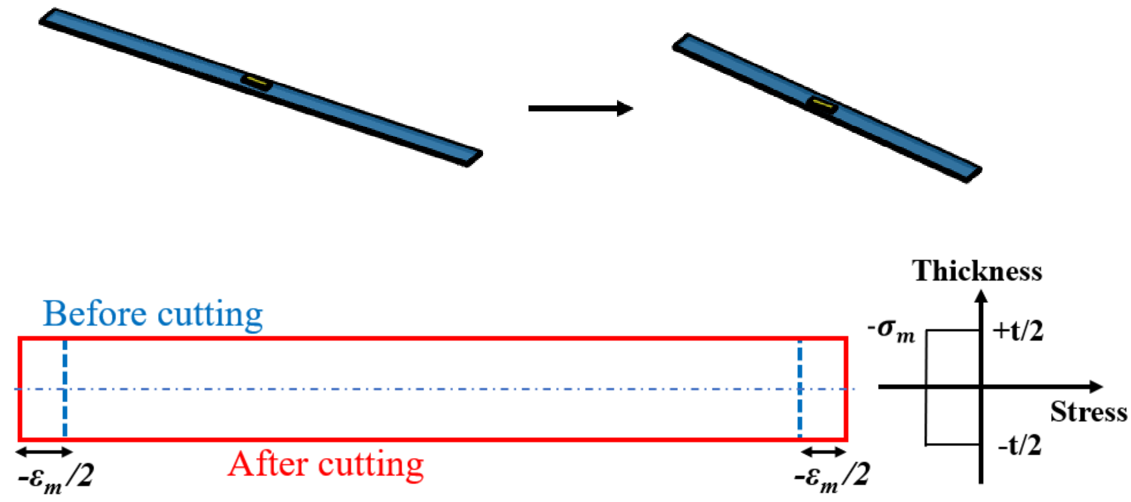

(b) Membrane residual stress

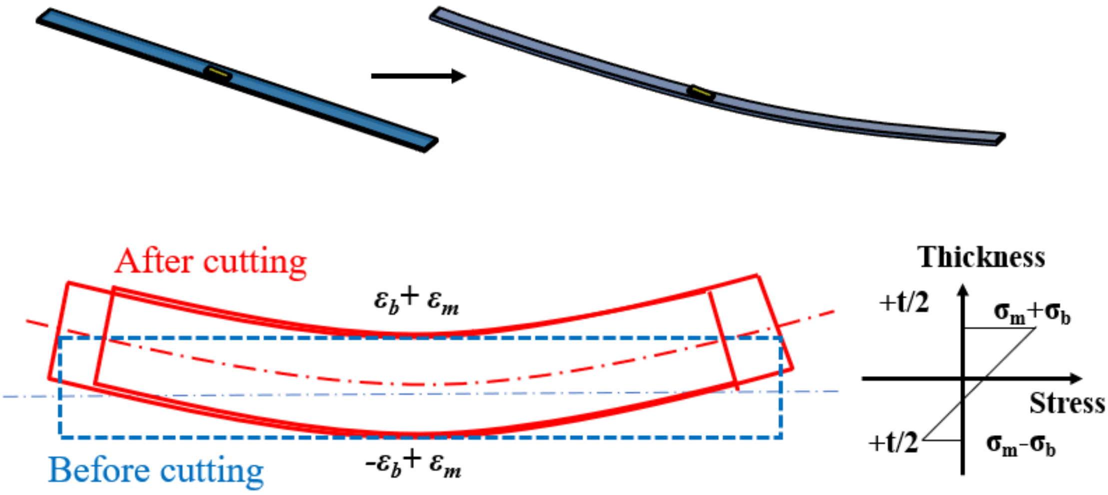

(c) Combined bending and tensile membrane residual stresses

Fig.21 Effects of membrane and bending residual stresses

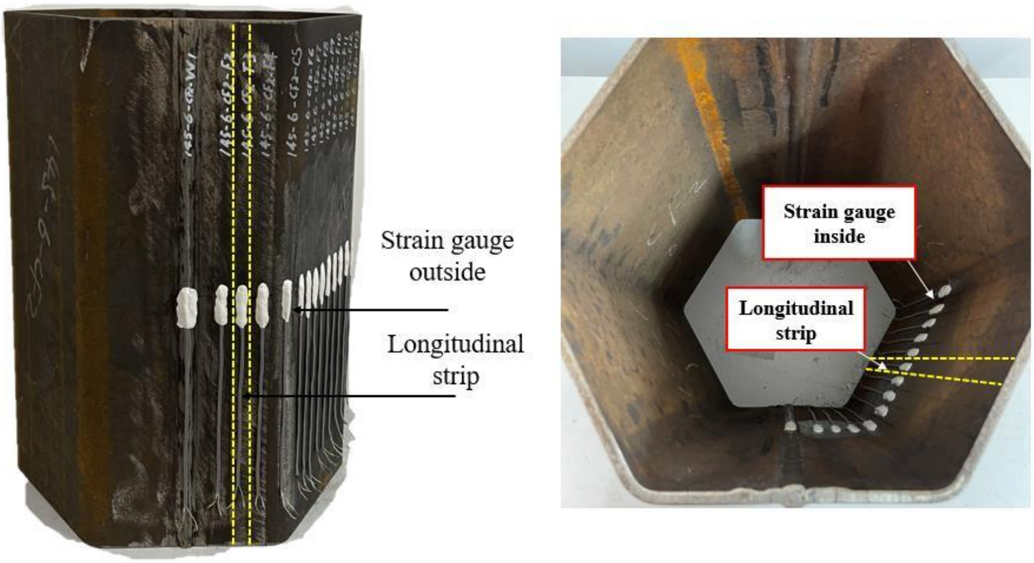

Fig. 22 Prepared specimen with outer and inner electric strain gauges ready for sectioning process

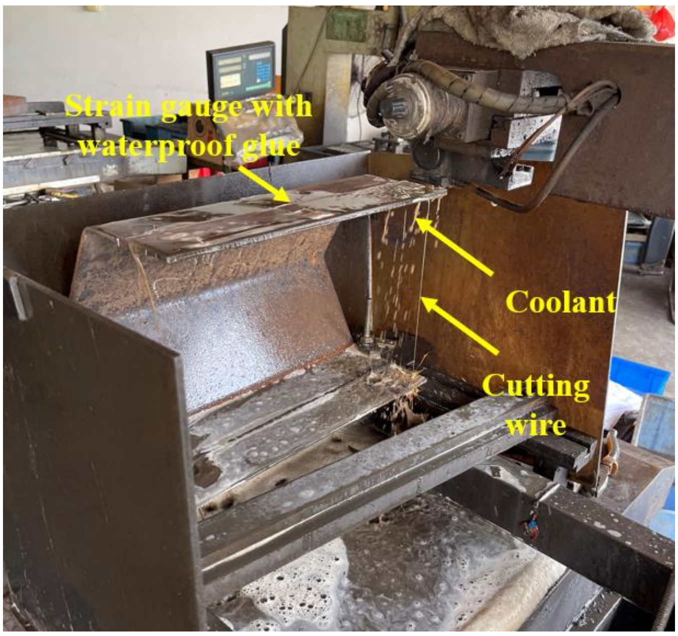

Fig. 23 Sectioning process using wire-cutting with coolant

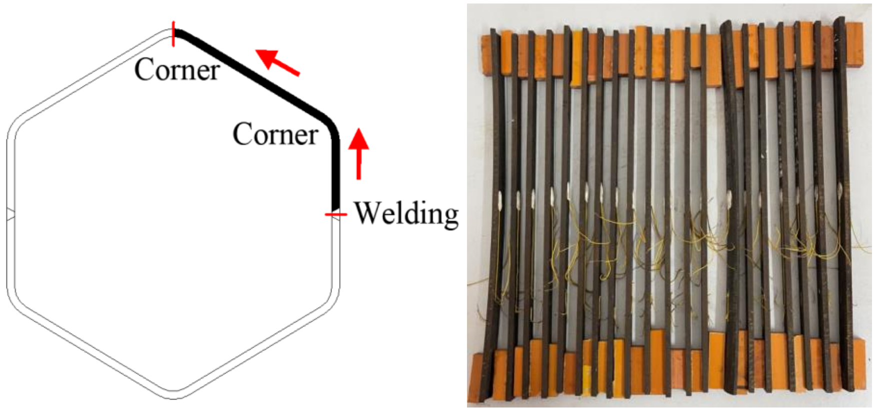

Fig. 24 Deformed strips from CF2-145 × 6 after sectioning process

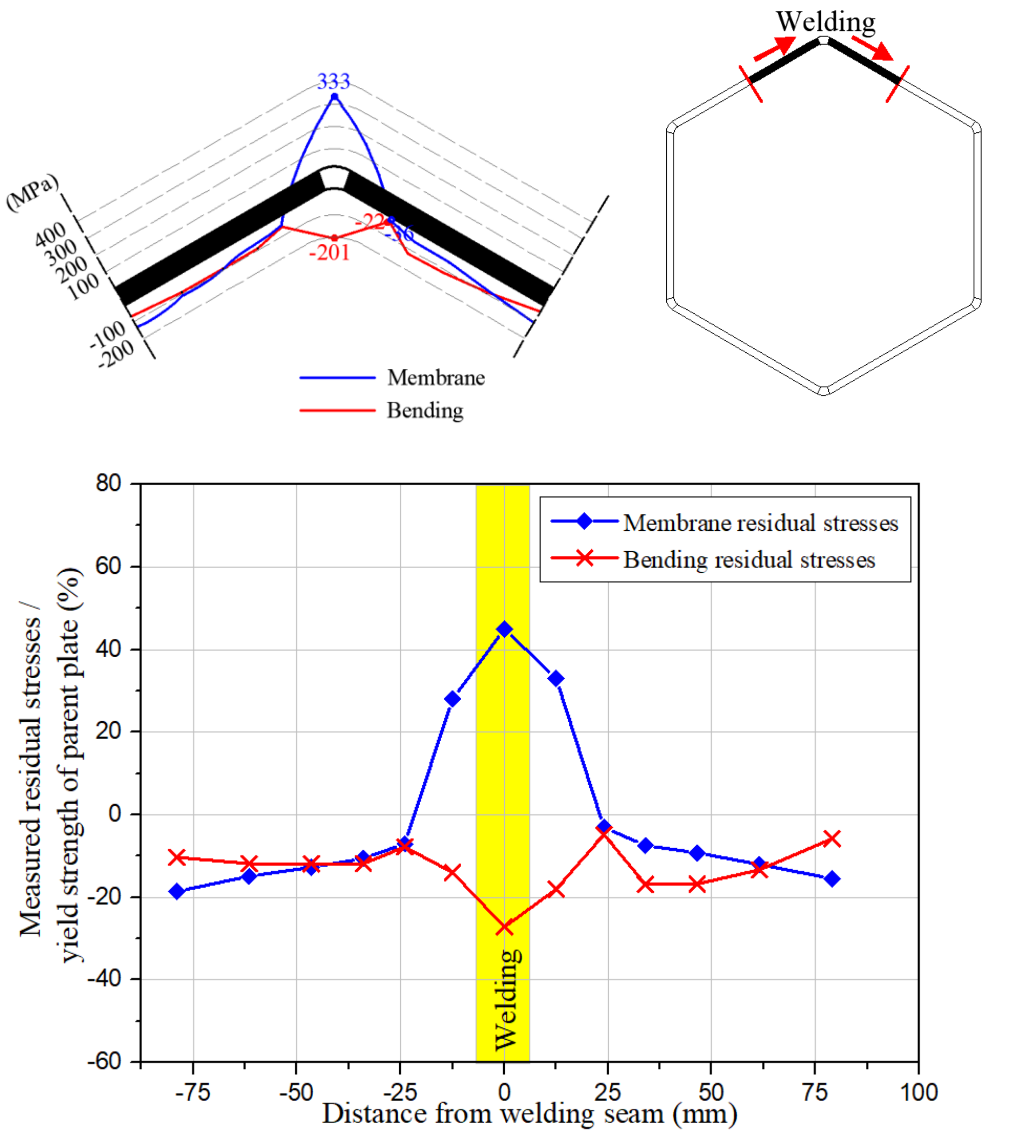

Fig. 25 Magnitude and the distribution of the longitudinal residual stresses in W-145 × 6

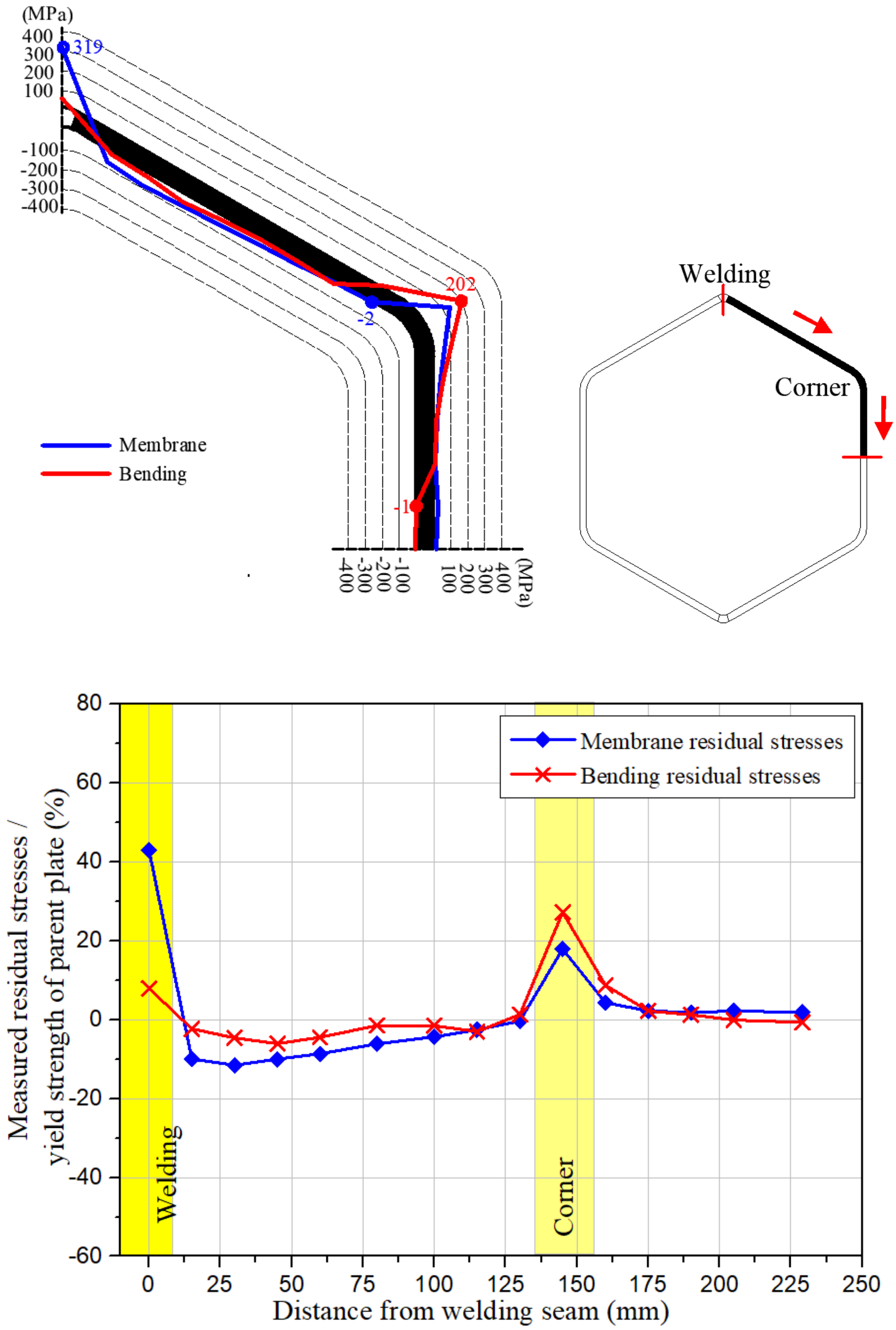

Fig. 26 Magnitude and the distribution of the longitudinal residual stresses in CF1-145 × 6

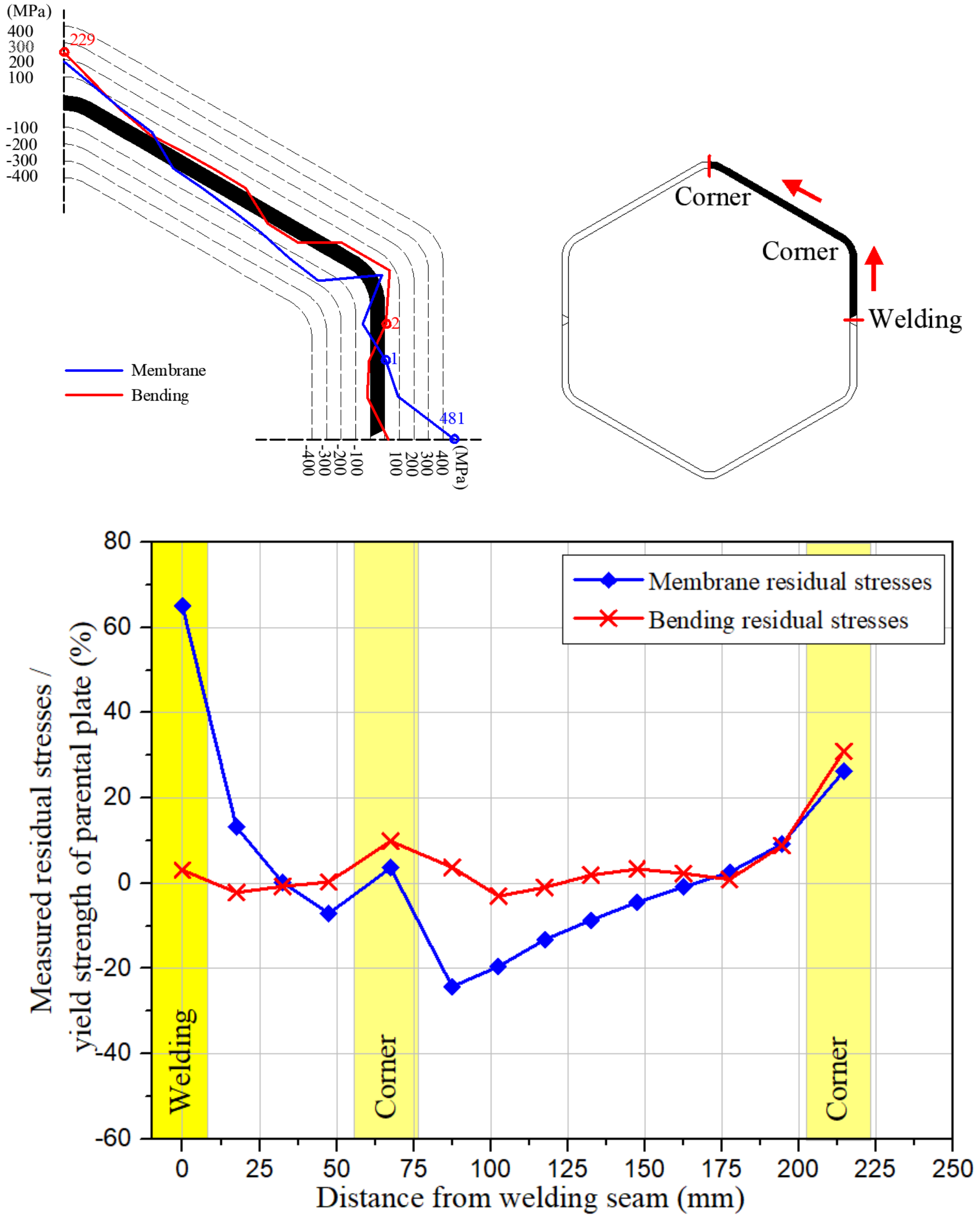

Fig. 27 Magnitude and the distribution of the longitudinal residual stresses in CF2-145 × 6

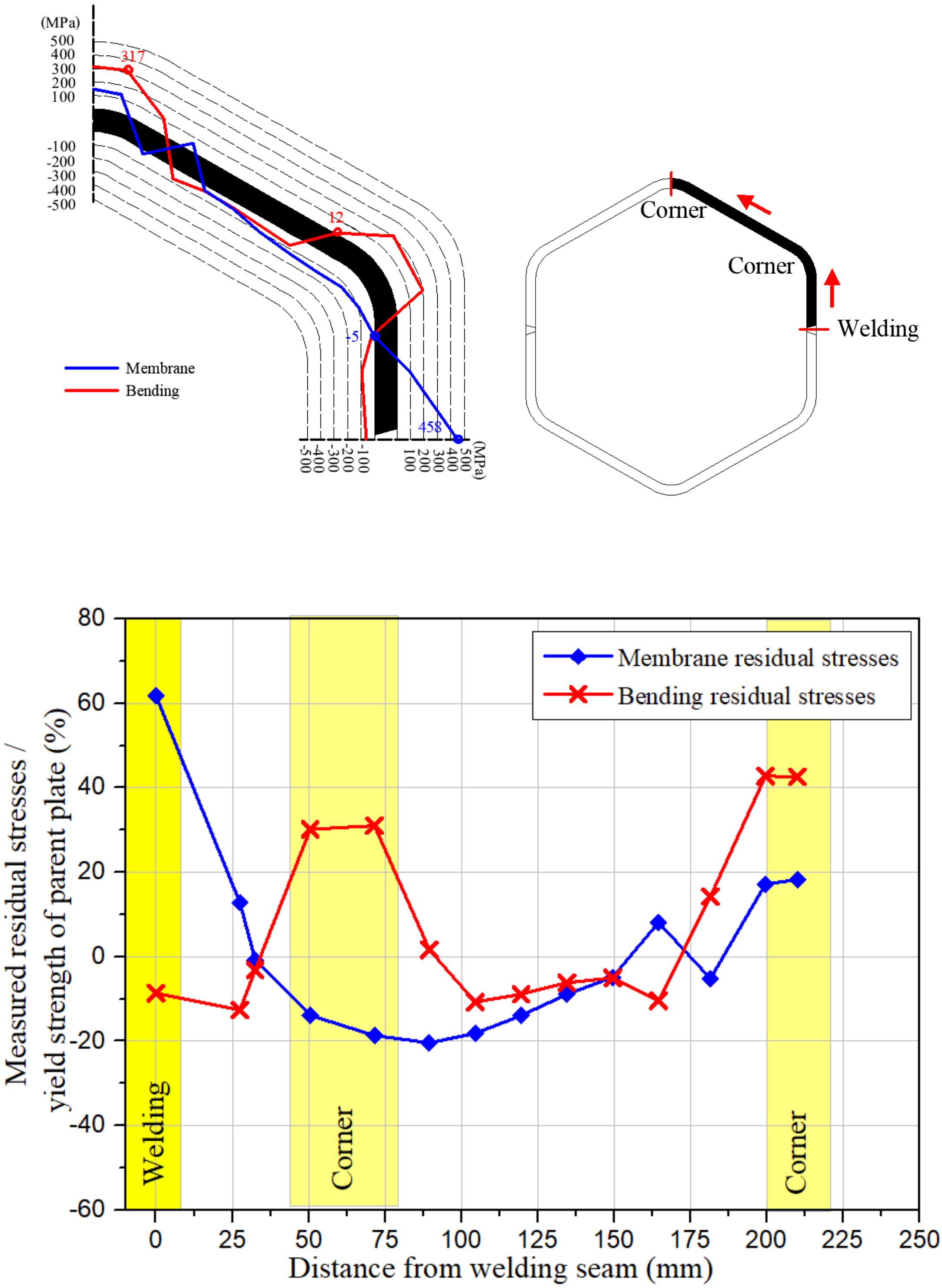

Fig. 28 Magnitude and the distribution of the longitudinal residual stresses in CF2-145 × 10

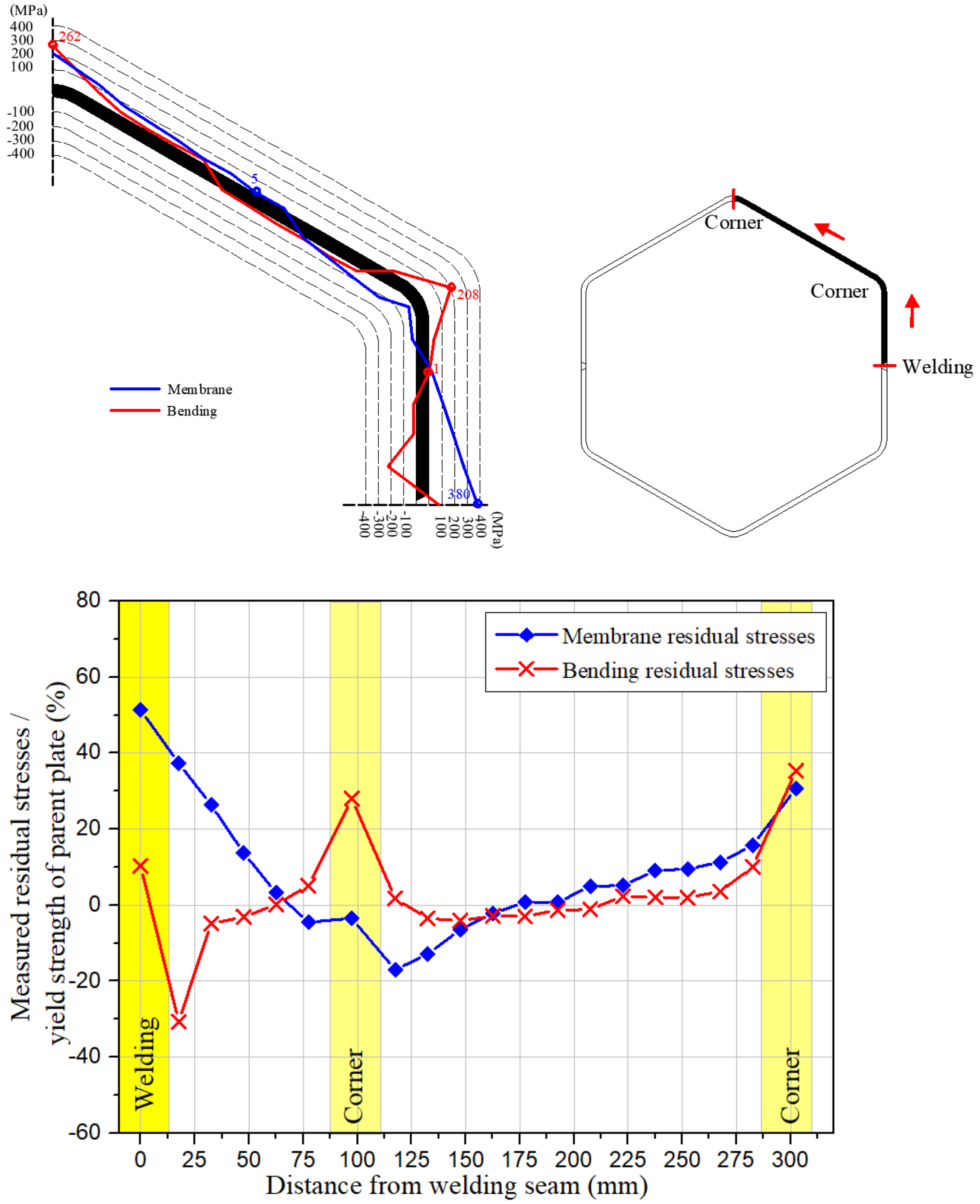

Fig. 29 Magnitude and the distribution of the longitudinal residual stresses in CF2-200 × 6

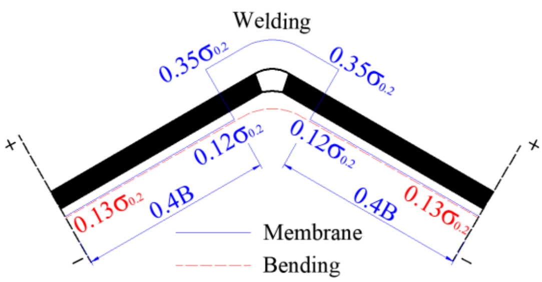

Fig. 30 Residual stress predictive model for W-series hexagonal hollow sections

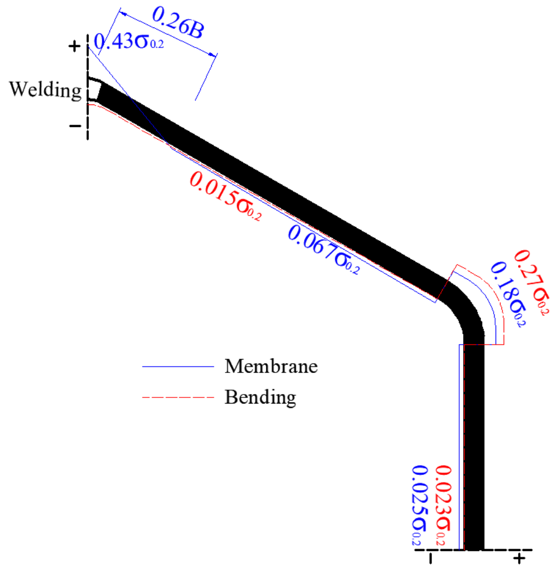

Fig. 31 Residual stress predictive model for CF1-series hexagonal hollow sections

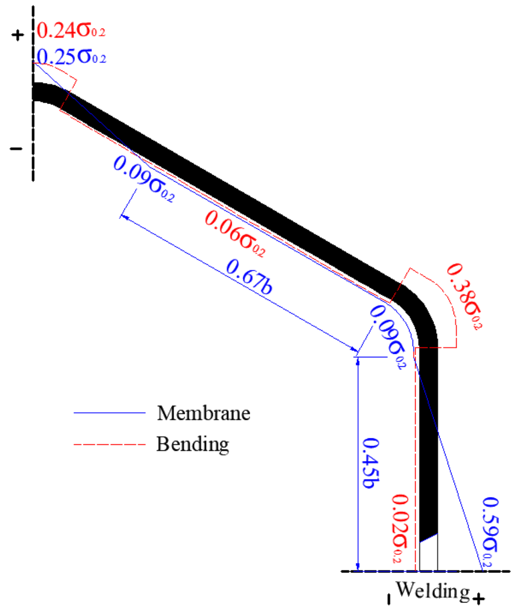

Fig. 32 Residual stress predictive model for CF2-series hexagonal hollow sections

Table 1 Chemical compositions listed in the mill certificates.

Steel plate	Chemical composition (wt%)										
	C	Mn	P	S	Si	Cr	Mo	Nb	Ti	B	CEV
6 mm plate	0.13	1.39	0.011	0.001	0.26	0.27	0.14	0.027	0.015	0.002	0.45
10 mm plate	0.14	1.41	0.012	0.001	0.26	0.26	0.15	0.025	0.014	0.002	0.46
EN 10025-6*	0.22	1.80	0.025	0.012	0.86	1.60	0.74	0.07	0.07	0.006	0.65

* Upper limit is listed

Table 2 Dimensions of hexagonal hollow section specimens.

Specimens	Edge length B (mm)	Side width b (mm)	Thickness t (mm)	Outer radius r_o (mm)	Inner radius r_i (mm)	b/t
W-145×6	146.0	125	5.78	24.6	18.5	21.6
CF1-145×6	145.7	124	5.85	24.8	18.4	21.2
CF2-145×6	146.7	119	5.86	24.5	18.7	20.3
CF2-200×6	201.7	178	5.88	25.2	18.8	30.3
CF2145×10	146.8	123	9.78	41.2	30.5	12.6

Table 3 Chemical composition of the welding electrode ER110S-G.

C	Mn	P	S	Si	Cr	Mo	Nb	Ti	V	Ni
0.09%	1.70%	0.009%	0.008%	0.70%	0.30%	0.60%	0.027%	0.1%	0.03%	1.85%

Table 4 Tolerance on radius to thickness ratios given in international specifications.

Specification or recommendation		Thickness t (mm)	Inner corner radius r_{in}	Outer corner radius r_{out}: Low alloy steel (yield strength higher than 390 MPa)	Outer corner radius r_{out}: Mild steel (yield strength lower than 320 MPa)
EN 10219-2 (CEN 2006) [105]		t≤6	0.6 t to 1.4 t	1.6 t to 2.4 t	
		t<6≤10	1.0 t to 2.0 t	2.0 t to 3.0 t	
ASTM A500 [106]		All t	≤2.0 t	≤3.0 t	
ASTM A1085 [107]		t ≤ 10.2	0.6 t to 2.0 t	1.6 t to 3.0 t	
		t>10.2	0.8 t to 2.0 t	1.8 t to 3.0 t	
GB/T 6728 (SAC 2017) [108]		3<t≤6	1.0 t to 2.0 t	2.0 t to 3.0 t	1.5 t to 2.5 t
		6<t≤10	1.0 t to 2.5 t	2.0 t to 3.5 t	2.0 t to 3.5 t
AS/NZS 1163 [109]		Perimeter equal or smaller than 50*50 mm	0.5 t to 2.0 t	1.5 t to 3.0 t	
		Larger than 50*50 mm	0.8 t to 2.0 t	1.8 t to 3.0 t	
JIS G 3101 (JSA 2015) [110]		3<t≤5 5<t≤16	2.0 t	3.0 t	0.5 t to 2.0 t
JIS G 3128 (JSA 2009) [111]		≤ 32	1.5 t	2.5 t	
		≥32	2.0 t	3.0 t	
JIS G 3466 [112]		All t	≤2.0 t	≤3.0 t	
CSA G40.20-13 [113]		3<t≤4	≤4.0 mm	≤8.0 mm	
		4<t≤5	≤10.0 mm	≤15.0 mm	
		5<t≤6	≤12.0 mm	≤18.0 mm	
		6<t≤8	≤15.0-16.0 mm	≤21.0-24.0 mm	
		8<t≤10	≤19.0-20.0 mm	≤27.0-30.0 mm	
SSAB [114]	Strenx 700	t<15	≥1.0 t	≥2.0 t	
		t ≥ 15	≥1.5 t	≥2.5 t	
	Strenx 900	t<20	≥2.0 t	≥3.0 t	
		t ≥ 20	≥2.5 t	≥3.5 t	
ISO 14346 (BSI 2013 [115]		2.5<t≤ 6	≥1.0 t	≥2.0 t	
		6<t≤10	≥1.5 t	≥2.5 t	

Table 5 Test results of the coupon specimens taken from the HSS hexagonal cross section - W-145×6. Note: * indicates the strain hardening was not observed from the tensile coupon test.

Section	E_s (GPa)	f_y (MPa)	f_u (MPa)	ε_u (%)	$\varepsilon_{f,ex}$ (%)	ε_f (%)	ε_{sh} (%)	$f_{0.05}$ (MPa)
W-145×6-F1	211.2	758	806	6.6	15.8	15.5	2.24	^
W-145×6-F2	209.4	762	802	6.8	16.5	16.2	*	756
W-145×6-W3	192.3	682	842	7.2	18.1	17.5	*	^
W-145×6-F4	214.5	766	805	6.7	17.2	15.6	1.86	^
W-145×6-F5	206.1	745	797	6.4	16.2	15.8	1.75	^

^indicates that the 0.05% proof strength is not applicable to the coupon with either welding materials or yield plateau

Table 6 Test results of the coupon specimens taken from the HSS hexagonal cross section - CF1-145× 6.

Section	E_s (GPa)	f_y (MPa)	f_u (MPa)	ε_u (%)	$\varepsilon_{f,ex}$ (%)	ε_f (%)	ε_{sh} (%)	$f_{0.05}$ (MPa)
CF1-145×6-W1	190.3	662	838	8.5	18.6	17.8	*	^
CF1-145×6-F2	197.1	752	793	5.9	19.4	18.8	1.15	^
CF1-145×6-F3	206.5	755	790	6	17.7	16.8	*	742
CF1-145×6-F4	221.1	762	802	6.2	16.9	17.2	2.02	^
CF1-145×6-C5	190.1	798	847	1.4	11.5	10.8	*	742
CF1-145×6-F6	209.4	755	806	6.5	16.8	15.9	*	740
CF1-145×6-F7	208.1	760	810	6.4	17.7	16.9	*	750

Note: * indicates the strain hardening was not observed from the tensile coupon test.

^indicates that the 0.05% proof strength is not applicable to the coupon with either welding materials or yield plateau

Table 7 Test results of the coupon specimens taken from the HSS hexagonal cross section – CF2-

145× 6.

Section	E_s (GPa)	f_y (MPa)	f_u (MPa)	ε_u (%)	$\varepsilon_{f,ex}$ (%)	ε_f (%)	ε_{sh} (%)	$f_{0.05}$ (MPa)
CF2-145×6-W1-	188.6	658	821	7.2	17.8	17.2	*	^
CF2-145×6-F2	206.8	755	798	7.0	19.6	17.3	2.1	^
CF2-145×6-F3	205.3	748	803	5.4	16.3	17.5	*	736
CF2-145×6-C4	191.0	792	858	1.2	10.3	11.6	*	741
CF2-145×6-F5	202.9	752	806	6.1	13.3	15.8	*	745
CF2-145×6-F6	211.2	760	802	6.8	16.2	16.5	1.95	^
CF2-145×6-F7	208.4	758	799	6.1	16.8	17.2	*	745
CF2-145×6-C8	189.9	795	855	1.3	10.9	11.2	*	732

Note: * indicates the strain hardening was not observed from the tensile coupon test.

^indicates that the 0.05% proof strength is not applicable to the coupon with either welding materials or yield plateau

Table 8 Test results of the coupon specimens taken from the HSS hexagonal cross section – CF2-200× 6.

Section	E_s (GPa)	f_y (MPa)	f_u (MPa)	ε_u (%)	$\varepsilon_{f,ex}$ (%)	ε_f (%)	ε_{sh} (%)	$f_{0.05}$ (MPa)
CF2-200×6-W1-	188.5	642	835	7.6	17.6	16.2	*	^
CF2-200×6-F2	211.4	770	810	6.4	18.1	17.5	2.15	^
CF2-200×6-F3	210.1	758	808	6.2	#	15.8	*	750
CF2-200×6-C4	193.2	788	868	2.0	14.2	11.6	*	721
CF2-200×6-F5	210.5	760	815	6.9	19.4	17.2	*	758
CF2-200×6-F6	215.7	762	812	5.9	12.8	15.3	*	752
CF2-200×6-F7	211.6	760	812	6.9	19.4	17.8	*	752
CF2-200×6-C8	191.5	792	860	2.1	12.8	10.8	*	743

Note: * indicates the strain hardening was not observed from the tensile coupon test.

# indicates that the fracture occurred outside the extensometer gauge length, thus $\varepsilon_{f,ex}$ was not obtained.

^indicates that the 0.05% proof strength is not applicable to the coupon with either welding materials or yield plateau

Table 9 Test results of the coupon specimens taken from the HSS hexagonal cross section – CF2-145× 10.

Section	E_s (GPa)	f_y (MPa)	f_u (MPa)	ε_u (%)	$\varepsilon_{f,ex}$ (%)	ε_f (%)	ε_{sh} (%)	$f_{0.05}$ (MPa)
CF2-145×10-W1-	193.8	662	834	7.8	18.2	17.1	*	^
CF2-145×10-F2	212.6	763	813	6.7	17.6	16.2	2.51	^
CF2-145×10-C3	198.2	792	842	1.8	12.2	13.2	*	732
CF2-145×10-F4	215.2	762	812	6.5	16.8	17.3	2.65	^
CF2-145×10-F5	206.2	768	810	5.1	15.5	16.6	*	765
CF2-145×10-C6	201.2	803	862	1.7	11.5	11.8	*	726

Note: * indicates the strain hardening was not observed from the tensile coupon test.
^indicates that the 0.05% proof strength is not applicable to the coupon with either welding materials or yield plateau

Table 10 Test results of the flat coupon specimens taken from the HSS parental plate with thickness of 6 mm.

Section	$E_{s,p}$ (GPa)	v	$f_{y,p}$ (MPa)	$f_{u,p}$ (MPa)	$\varepsilon_{u,p}$ (%)	$\varepsilon_{f,p}$ (%)	$\varepsilon_{f,ex}$ (%)	$\varepsilon_{sh,p}$ (%)
6 mm plate-L1	214.8	0.29	753	809	6.3	15.1	15.4	*
6 mm plate-L2	212.3	0.28	757	808	6.6	14.7	15.8	*
6 mm plate-L3	215.2	0.30	756	807	6.4	14.2	15.3	*
6 mm plate-T1	213.2	0.29	762	808	6.5	15.2	#	2.1
6 mm plate-T2	214.6	0.29	767	809	6.2	14.8	15.2	2.2
6 mm plate-T3	214.3	0.30	763	805	6.7	15.7	15.3	1.65

Note: * indicates the strain hardening was not observed from the tensile coupon test.
# indicates that the fracture occurred outside the extensometer gauge length, thus $\varepsilon_{f,ex}$ was not obtained.

Table 11 Test results of the flat coupon specimens taken from the HSS parental plate with thickness of 10 mm.

Section	$E_{s,p}$ (GPa)	v	$f_{y,p}$ (MPa)	$f_{u,p}$ (MPa)	$\varepsilon_{u,p}$ (%)	$\varepsilon_{f,p}$ (%)	$\varepsilon_{f,ex}$ (%)	$\varepsilon_{sh,p}$ (%)
10 mm plate-L1	215.2	0.31	752	803	6.5	15.9	16.9	2.3
10 mm plate-L2	214.6	0.30	762	809	6.7	16.7	17.8	2.5
10 mm plate-L3	216.8	0.32	754	812	6.6	16.5	17.1	2.5
10 mm plate-T1	215.6	0.28	763	808	6.4	15.3	15.6	2.28
10 mm plate-T2	216.3	0.29	752	806	6.6	16.9	18.6	2.1
10 mm plate-T3	218.2	0.30	763	802	6.5	15.8	17.9	2.26

Table 12 Measured material properties from corner coupon specimens for sections in CF1 and CF2 series and the predicted values using different methods.

Specimen	Experimental results		Prediction by Karren [43]		Prediction by Pham et al. [45]		Prediction by Gardner et al. [14]	
	f_y (MPa)	f_u (MPa)	$f_{y,c}$ (MPa)	$\frac{f_{y,c}}{f_y}$	$f_{y,c}$ (MPa)	$\frac{f_{y,c}}{f_y}$	$f_{y,c}$ (MPa)	$\frac{f_{y,c}}{f_y}$
CF1-145×6-C5	798	847	827	1.04	877	1.10	728	0.91
CF2-145×6-C4	792	858	846	1.07	880	1.11	737	0.93
CF2-145×6-C8	795	855	840	1.06	880	1.11	735	0.92
CF2-200×6-C4	788	868	862	1.09	882	1.12	744	0.94
CF2-200×6-C8	792	860	849	1.07	881	1.11	738	0.93
CF2-145×10-C3	792	842	823	1.04	871	1.10	724	0.91
CF2-145×10-C6	803	862	847	1.05	888	1.11	741	0.92
			Mean	1.06	Mean	1.11	Mean	0.93
			CoV	0.017	CoV	0.006	CoV	0.011

Table 13 Summary of material test results for the steel with $f_{y,nom}$ = 690-700 MPa.

References	Steel grade	Full stress-strain curves	Material parameters f_y,f_u and ε_u
McDermott [64]	A514	/ (I-sections)	36
Rasmussen and Hancock [65]	BISALLOY 80	2 (Box and I-sections)	6
Yuan [66]	700Q	1 (W-sections)	3
Salem and Sause [67]	HPS 100W	5 (I sections)	15
Tang [68]	BISPLATE-80	2 (I-sections)	69
Coelho et al. [69]	S690	/ (I-sections)	6
Shi et al. [70]	S700MC and S690QL1	/ (I-sections)	12
Yan et al. [71]	RQT701	1 (Sheets)	/
Xue [72]	Q690GJ	2 (Box and I-sections)	/
Chiew et al. [73]	S690	1 (Sheets)	/
Chen et al. [74]	Q690D	/ (H-sections)	15
Li et al. [75]	Q690	1 (Box and H-sections)	15
Wang et al. [76]	Q690D	2 (Sheets)	15
Wang et al. [77]	S690	1 (SHS[1] and RHS[2])	15
Ma et al. [78]	S690	9 (H-sections)	27
Zhang [79]	Q690	2 (H-sections)	27
Hao [80]	Q690D	1 (Sheets)	24
Liu [81]	S690	12 (H-sections)	120
Peng [82]	Q690D	3 (H-sections)	27
Hai et al. [83]	Q690D	10 (Sheets)	9
Wang [84]	S690	5 (H-sections)	15
Huang et al. [85]	Q690	2 (Sheets)	/
Ho et al. [86]	S690	2 (Sheets)	18
Fang et al. [21]	S690	9 (OctHS[4])	132
Sun et al. [87]	S700MC	2 (I-sections)	6
Huang et al. [98]	BISALLOY 80	Box and I-sections	1
Lai et al. [89]	S690	4 (Sheets)	/
Sun at al. [90]	Q690	1 (Connections)	18
Ho et al. [43]	S690	/ (Sheets)	6
Amraei et al. [91]	S700	/ (Sheets)	3
Zhang et al. [92]	S690	12 (Angle and channels)	54
Le et al. [93]	BISPLATE-80	2 (I-sections)	6
Guo et al. [94]	S690	1 (Sheets)	6
Su et al. [95]	S700MC	2 (I-sections)	/
Ho et al. [96]	S690	5 (Sheets)	90
Hu et al. [97]	S690	1 (Sheets)	9
Zhang et al. [98]	Q690	1 (Sheets)	9

Cadoni and Forni [99]	S690QL	2 (Sheets)	6
Chung et al. [100]	S690	1 (H-sections)	21
Wang and Lui [101]	Q690	1 (Sheets)	/
Chen and Chan [61]	Q690	1 (CHS[3])	3
Lin et al. [102]	Q690	2 (Connections)	6
Yang et al. [103]	Q690	3 (I-sections)	9
Bartsch et al. [104]	S690	4 (Sheets)	6
Total		142	855

Note that: /: the information is unavailable in the literature. [1]: indicates square hollow section and [2]: means rectangle hollow section [3]: implies circular hollow section and [4] indicates octagonal hollow section